Post-seismic deformation following the June 2000 earthquake sequence in the South Iceland Seismic Zone

Thóra Árnadóttir[1], Sigurjón Jónsson[2], Fred F. Pollitz[3], Weiping Jiang[1], and Kurt L. Feigl[4]

Short title: POST-SEISMIC DEFORMATION IN THE SISZ

Abstract.

We observe post-seismic deformation on two spatio-temporal scales following M_w=6.5 earthquakes in the south Iceland seismic zone on June 17 and 21, 2000. We see a rapidly decaying deformation transient lasting no more than 2 months and extending about 5 km away from the two mainshock ruptures. This local, month-scale transient is captured by several radar interferograms (InSAR) and is also observed at a few campaign GPS sites located near the faults. A longer-scale transient with a characteristic time scale of about a year is only detected by GPS measurements. The month-scale deformation pattern has been explained by poro-elastic rebound due to post-earthquake pore-pressure changes [*Jónsson et al.,* 2003]. In contrast, the year-scale deformation can be explained by either afterslip at 8–14 km depth or viscoelastic relaxation of the lower crust and upper mantle in response to the coseismic stress changes. The optimal viscoelastic models have lower crustal viscosities of 0.5–1 $\times 10^{19}$ Pa s and upper mantle viscosity $\sim 3 \times 10^{18}$ Pa s. Due to the limitations of our GPS campaign data we consider both afterslip and viscoelastic relaxation as plausible mechanism explaining the deformation field. Both types of post-seismic deformation models suggest that the areas of large co-seismic stress increase east of the June 17 and west of the June 21 ruptures, continue to be loaded by the post-seismic deformation.

1. Introduction

The plate spreading across south Iceland is accommodated by rifting in the eastern volcanic zone (EVZ), and to a lesser extent the western volcanic zone (WVZ), and left-lateral E–W transform motion across the south Iceland seismic zone (SISZ), that connects the two volcanic zones (Figure 1). The relative plate motion across the SISZ is facilitated by right–lateral strike slip motion on many parallel N–S oriented faults, rather than one E–W transform fault [*Einarsson and Eiríksson,* 1982; *Einarsson et al.,* 1981]. Sequences of large earthquakes ($M_S \geq 6$) lasting over a time period of days to years have occurred in the SISZ in historical time in Iceland (last 1100 years). Typically, they start with an earthquake in the eastern part of the SISZ and continue with events of equal or smaller magnitude further west. The time interval between large earthquake sequences in the SISZ ranges between 45 and 112 years [*Einarsson et al.,* 1981], with the most recent one in June 2000. Large localized events have also occurred in the eastern and western ends of the SISZ, the only instrumentally recorded of these was a M_S=7.0 in 1912 [*Bjarnason et al.,* 1993a], located in the eastern part of the zone.

Figure 1

The June 2000 sequence started with a magnitude M_w=6.5 earthquake on June 17, 2000 [*Dziewonski et al.,* 2001; *Stefánsson et al.,* 2003]. Seismicity increased over a large area in SW Iceland following the June 17 mainshock, with three M≥5 events triggered on Reykjanes Peninsula [*Pagli et al.,* 2003; *Clifton et al.,* 2003; *Árnadóttir et al.,* 2004] (Figure 1). A second large magnitude (M_w=6.5) event occurred on June 21, 2000 [*Dziewonski et al.,* 2001; *Stefánsson et al.,* 2003], located about 17 km west of the

June 17 rupture (Figure 1). Signals from the earthquakes were detected by several local networks: the South Iceland Lowland (SIL) digital seismic network, a strong motion network, a volumetric strain meter network, and the continuous GPS network in Iceland. The earthquakes caused significant pressure changes in geothermal reservoirs over an extensive area [*Björnsson et al.,* 2001] with local changes correlating well with the focal mechanisms of the two largest events. Surface faulting was observed for the events in the SISZ and on Reykjanes Peninsula, indicating rupture on N–S trending faults [*Clifton et al.,* 2003; *Clifton and Einarsson,* 2005]. The coseismic crustal deformation caused by the two earthquakes was measured with both network GPS [*Árnadóttir et al.,* 2001] and interferometric synthetic aperture radar (InSAR) [*Pedersen et al.,* 2001]. These studies used the geodetic data to estimate fault geometries assuming uniform or simple slip models. In a subsequent study the InSAR and GPS data were combined to estimate the best fit fault geometries and distributed slip models for the two mainshocks [*Pedersen et al.,* 2003].

The June 2000 earthquake sequence provides the first opportunity to study post-seismic deformation in Iceland. In this study we concentrate on the long term post-seismic deformation field observed by annual GPS campaigns from 2000 to 2004. To isolate post-seismic signals in the observed velocity fields, we correct for the effect of plate spreading, using an interseismic velocity field estimated from pre-seismic GPS observations. The first months of post-seismic deformation contain signals due to post-seismic ground water movements inferred from InSAR measurements [*Jónsson et al.,* 2003]. We use the poro-elastic relaxation model from *Jónsson et al.* [2003] to correct

the 2000–2001 GPS velocity field. The resulting GPS velocities are then compared to model predictions from bulk viscoelastic relaxation in the lower crust and upper mantle and from afterslip on discrete rupture surfaces below the coseismic ruptures. The signal in the vertical GPS velocity field is marginally above the measurement error and can therefore not be used as a discriminant between afterslip and viscoelastic models.

2. GPS measurements and data analysis

The GPS network in the south Iceland seismic zone has been re-measured every year following the June 2000 earthquakes (Figure 1). The 2000 survey was carried out between June 19 and July 3 when a total of 39 stations were observed, and each site was occupied for at least three 8 hour sessions. Seven stations were observed before the June 21 earthquake, and repeated after the event. In the later surveys, each site was occupied for 2 to 4 days, with at least one 24 hr session and two sessions less than 24 hours. All the surveys were performed using dual-frequency GPS receivers, collecting data every 15 s. The next two surveys took place on June 20 to July 19, 2001 (43 stations) and on October 2 to 28, 2002 (44 stations). The 2003 survey was carried out in two parts. The western part of the network was surveyed from June 25 to July 2, and the eastern part (with six stations reoccupied from the June survey) during September 14–27 (54 stations in total). The survey in 2004 included 41 stations and took place from May 3–14.

We have analysed all campaign and continuous GPS data collected in the SISZ from 1992–2004 using the GAMIT/GLOBK software [*King and Bock,* 2003; *Herring,*

2003]. The analysis produces three-component time series of daily station positions with respect to the ITRF2000 reference frame [*Altamimi et al.,* 2002]. The solution describes station motions in terms of absolute velocities and displacements. The velocities represent the average velocity, equivalent to the slope of the position time series estimated from the GPS observations. The details of the analysis are discussed in a separate study [*Árnadóttir et al.,* submitted, 2005]. We estimate station velocities for the pre-seismic time interval (1992–2000), several year-long post-seismic intervals, and a longer interval from June 2001 through May 2004. The GPS station velocities for the time intervals 1992–2000, 2000–2001 and 2001-2004 are given in Tables 1–3 (electronic supplement [1]). Although the formal uncertainties given here have not been scaled by any *a posteriori* estimate of variance, previous studies using the same approach indicate that they adequately reflect the data scatter [*e.g., McClusky et al.*, 2000].

3. Interseismic GPS velocity field in the SISZ

We estimate a surface velocity field in SW Iceland, representing the background secular motion in the area, using GPS campaign observations from 1992–1999 (Figure 2) [*Sigmundsson et al.,* 1995; *Árnadóttir et al.,* submitted, 2005]. Unfortunately, this velocity field is perturbed in the area around Hengill volcano due to an inflation during 1993–1998 [*Sigmundsson et al.,* 1997; *Feigl et al.,* 2000]. Two continous GPS stations,

Figure 2

[1]Supporting material is available via Web browser or via Anonymous FTP from "ftp://ftp.agu.org/apend/" (Username = "anonymous", Password = "guest").

HVER and OLKE, were installed in the Hengill area in early 1999. These stations show slower velocities, calculated from data spanning 1999–2000, than the campaign stations 5 to 10 km farther east. This indicates that the inflation period at Hengill ended sometime in late 1998 to early 1999. A model assuming a point source of inflation at ∼7 km depth, fitting a rate of uplift of 19 mm/yr obtained from InSAR data spanning 1993–1998 [*Feigl et al.,* 2000], predicts small horizontal velocities in the western part of the SISZ due to the Hengill inflation (white arrows in Figure 2). We therefore neglect the stations near Hengill to estimate a smooth pre-seismic velocity field.

Not all the GPS stations were occupied on two separate occasions before the earthquakes in 2000. Interseismic horizontal velocities at these stations were estimated by interpolation (Delaunay triangulation) of neighboring station velocities with pre-seismic uncertainties lower than 4 mm/yr. This procedure yields a smooth pre-seismic velocity field that is valid even for the stations affected by the 1993–1998 inflation episode at Hengill (shown with white arrows in Figure 3 and Table 1, electronic supplement). A similar interpolation of the vertical pre-seismic velocity field is not possible due to the large uncertainties in the velocity estimates and perturbations caused by the Hengill inflation prior to the June 2000 earthquake sequence. The details of the pre-seismic velocity field in SW Iceland are described in a separate study [*Árnadóttir et al.,* submitted, 2005].

Figure 3

4. Post-seismic velocities in the SISZ

We correct the post-seismic velocities for secular plate motion by subtracting the estimated interseismic horizontal velocity field from the year-to-year solutions. We therefore assume that the background plate spreading was not perturbed by the earthquakes and remains unchanged during the post-seismic interval. We do not, however, make a similar correction to the vertical velocities as we do not have vertical velocities for the pre-seismic interval at most of our stations in the SISZ. The vertical velocities shown in figures are in the ITRF2000 reference frame. The signal-to-noise ratio of the annual post-seismic velocities is low as the remaining signal is small after subtracting the interseismic motion (Figure 4). In addition, the velocity estimates appear to be rather variable from one year to another, *e.g.,* for the 2002–2003 and 2003–2004 intervals, where the time between the observations is less than one year. Inspection of the post-seismic station time series suggests that the velocities are not decaying rapidly from 2001 to 2004. We therefore divide the post-seismic time series into two intervals; 2000–2001 when the post-seismic signal appears to be larger than for the other intervals, and 2001–2004 interval, when post-seismic velocities appear relatively stable (Figure 4). We use the velocities from these two time intervals in the remainder of this paper.

Figure 4

The general pattern of the post-seismic displacements has stations to the west of the June 21 rupture with a northward motion, turning more westward north of the two ruptures, while stations to the east of the June 17 rupture move southwest to southward

(Figure 4). Velocities of the stations in the area between the faults are small. The vertical velocity pattern is less clear, with most stations showing uplift. We exclude vertical data from the easternmost stations (THJO and ISAK) in our analysis as the high vertical velocity is probably due to re-inflation of the Hekla volcano following the February 2000 eruption.

5. Poro-elastic transient

A rapid post-seismic deformation transient was observed in satellite radar interferograms (InSAR) near the June 17 and June 21 surface ruptures during the first two months after the earthquakes [*Jónsson et al.,* 2003]. The InSAR data record changes in distance along the near-vertical line of sight between the ground and the ERS-2 satellite between June 19 and July 24. The observed deformation pattern shows four quadrants around the June 17 rupture (Figure 5a). Post-seismic subsidence is observed in the (co-seismic) compressive quadrants NW and SE of the ruptures, while post-seismic uplift is found in the extensional quadrants. The deformation decayed rapidly after the earthquakes and appears to have lasted about two months [*Jónsson et al.,* 2003].

Figure 5

The observed deformation signal cannot be explained by deep rooted mechanisms such as viscoelastic relaxation in the lower crust and upper mantle or by post-seismic afterslip occurring below the co-seismic fault slip [*Jónsson et al.,* 2003]. The deformation pattern is, however, consistent with models of poro-elastic rebound in the crust due to post-earthquake changes in pore-pressure (Figure 5b). For this model calculation

we assume a poro-elastic crust that changes from an undrained state (Poisson's ratio of $\nu_u = 0.31$) just after the earthquakes to a fully drained state ($\nu = 0.27$) where all the earthquake-induced groundwater pressure changes have dissipated. This model also assumes the co-seismic slip distributions estimated for the June 17 and 21 mainshocks from a joint inversion of the co-seismic GPS and InSAR measurements [*Pedersen et al.,* 2003]. Both the magnitude and pattern of the deformation predicted from this model agree well with the InSAR data (Figure 5a). In addition, this interpretation is supported by water-level observations from numerous geothermal wells in the region. The spatial distribution of the post-seismic water-level changes is consistent with the observed rebound and the water-level recovery in most wells also took about 1-2 months [*Jónsson et al.,* 2003].

We use this poro-elastic model to calculate predicted GPS displacements at our network stations and to correct the 2000–2001 GPS velocities for this effect. The largest predicted displacements are within 5 km of the fault ruptures and a significant part of the observed velocities at these stations can be explained by poro-elastic rebound (white arrows in Figure 4a and c and Table 4, electronic supplement). The vertical signal is less well correlated with the model than the horizontal, with some stations showing uplift where the model predicts subsidence. In particular at station AKBR, near the northern end of the June 17 fault where the model can only explain a fraction of the observed velocity, although the azimuth for the horizontal component is not far off. The poro-elastic deformation northwest of the June 17 rupture appears to have been unusually strong, possibly due to different crustal material properties, as here the model

also under-predicts the observed InSAR data (Figure 5c). This GPS station (AKBR) may also have been affected by anelastic deformation due to surface cracks observed close to the station and we therefore exclude it in our analysis below. For the remaining GPS stations we subtract the poro-elastic model predictions from the 2000–2001 velocity field. We use this corrected velocity field in our modeling of the longer term post-seismic deformation in the following sections.

6. Viscoelastic relaxation

To explain the year-scale transients observed in the post-seismic velocity fields, we explore a transient rheology. The simplest form of a transient rheology is a Burgers body, as shown in Figure 6. This is a linear biviscous model consisting of a Maxwell element in series with a Kelvin element. Five parameters are needed to parameterize the rheology of such a material: the steady-state shear modulus μ_1, the steady-state bulk modulus κ_1, the steady-state viscosity η_1, the transient shear modulus μ_2, and the transient viscosity η_2. This rheology allows for an initial transient response associated with relaxation time $\tau_2 = \eta_2/\mu_2$ followed by a slower steady-state response associated with relaxation time $\tau_1 = \eta_1/\mu_1$, for suitable choices of $\eta_2 << \eta_1$. The details of the equations governing the Burgers body are given by *Pollitz* [2003]. It is useful to note that the response at times that are long compared with τ_2 but short compared with τ_1 is equivalent to the elastic response with modified shear modulus $\mu' = \mu_1\mu_2/(\mu_1 + \mu_2)$. If either $\eta_2 = \infty$ or $\mu_2 = \infty$, the material behavior reduces to that of a Maxwell rheology. Several studies have used this type of transient rheology to describe crustal

Figure 6

deformation [*e.g., Peltier et al.*, 1981; *Yuen et al.*, 1986]. *Bills et al.* [1994] explored millenium scale crustal asthenosphere relaxation following unloading of lacustrine loads in the western US, employing a Burgers body rheology for the mantle. *Ivins* [1996] explored the possibility of transient rheology in the lower crust of the Mojave Desert, California in order to explain rapid post-seismic deformation observed for the first 3 months following the 1992 M=7.4 Landers earthquake. *Pollitz* [2003] examined the time-dependent GPS velocity field around the region of the 1999 M=7.1 Hector Mine, California earthquake, finding that both horizontal and vertical deformation patterns could be well explained by predominantly viscoelastic relaxation of the mantle, its rheology being a Burgers body with material relaxation times of 0.07 and 2 years. Unlike earlier crustal deformation studies, *Pollitz* [2003] isolated the transient rheology to be predominantly a mantle phenomenon, dominant over any possible transient rheology in the lower crust. A similar conclusion is reached by *Pollitz* [2005] in the area of the 2002 Denali, Alaska earthquake, where the temporal pattern and observation of anomalously rapid horizontal postseismic movements at great distance from the rupture again point to a transient rheology in the mantle. It is not clear if a transient rheology or a stress and temperature-dependent nonlinear rheology [*Freed and Bürgman,* 2004] best characterizes the mantle. It is also unknown if a transient rheology is applicable to Earth's upper mantle globally. It is, however, consistent with the expected initial rapid transient response followed by a transition from anelastic to viscous deformation mechanisms, based on laboratory constraints on transient rheology and corresponding constitutive relationships (*e.g., Minster and Anderson*, 1981).

The present SISZ dataset is not sufficient to independently constrain a transient rheology in Iceland. We therefore follow earlier studies and adopt a layered viscoelastic structure with a Maxwell rheology with viscosity η_c for the lower crust, and a Burgers body rheology with a steady state viscosity η_1 for the mantle below the SISZ (Figure 7). Figure 7 We assume an elastic upper crust down to 10 km, based on the depth extent of earthquake hypocenters in the SISZ [*e.g., Stefánsson et al.*, 1993; *Tryggvason et al.*, 2002], and a lower crust from 10–20 km consistent with estimates of Moho depth from seismic studies [*e.g., Bjarnason et al.*, 1993b; *Allen et al.*, 2002]. Based on inferred mantle rheology from previous studies applying a Burgers body rheology [*Pollitz*, 2003; *Pollitz*, 2005], we assume a transient mantle viscosity that scales with the steady state viscosity, such that $\eta_2 = \eta_1 \times 0.036$. We also assume that $\mu_2 = \mu_1$, then $\mu' = 0.5 \times \mu_1$.

Predicted viscoelastic relaxation is controlled by source models of the June 17 and June 21 events [*Árnadóttir et al.,* 2001] combined with the depth distribution of viscoelastic parameters. We employ the method of *Pollitz* [1997] to compute the globally valid viscoelastic surface deformation fields at specific points and given time interval. The model velocity field depends on both the viscoelastic parameters as well as a velocity shift:

$$\mathbf{v}_j(\mathbf{r}_i) = \mathbf{v}_j^{\mathrm{VE}}(\mathbf{r}_i) + \mathbf{\Delta v}_j \qquad (1)$$

where $\mathbf{v}_j(\mathbf{r}_i)$ is the total calculated surface velocity field at site i and time interval j, $\mathbf{v}_j^{\mathrm{VE}}(\mathbf{r}_i)$ is the contribution of viscoelastic relaxation, and $\mathbf{\Delta v}_j$ is the velocity shift

vector for that time interval. This velocity shift is meant to account for possible long-wavelength inaccuracies in the interseismic correction, including a background uplift signal.

For time interval j the misfit function is defined as

$$\chi^2{}_j = \mathbf{q}_j^T \cdot \mathbf{C}_j{}^{-1} \cdot \mathbf{q}_j \tag{2}$$

where, for each time interval j, the column vector $\mathbf{q}_j$ is obtained by taking the difference between the observed velocity field $\mathbf{u}_{ji}$ at site i and the model prediction $\mathbf{v}_j(\mathbf{r}_i)$ at that site, and $\mathbf{C}_j$ is the associated data covariance matrix. The residual vector $\mathbf{q}_j$ has 3 components from each site for a total of $3n$ components, where n is the total number of sites.

We generate different sets of models by varying both η_c and η_1 in a grid search for minimum-misfit models. Figure 8 shows the fit of model velocity fields to observed 2000–2001 and 2001–2004 velocity fields, separated into the horizontal and vertical components. The misfit for a given model is shown with respect to both η_c and η_1, the former being represented by the ratio η_c/η_1. A line with a slope of -1 on these plots represents models of constant η_c. For the horizontal velocity field it is clear that low-misfit models tend to fall on such a line, corresponding to $\eta_c \sim 0.5 - 1 \times 10^{19}$ Pa s and admissible η_1 over a broad range from 10^{18} to 10^{20} Pa s. Thus, even allowing for possible complexity in the mantle post-seismic response, we find that the horizontal GPS measurements following the June 17 and 21 SISZ events constrain lower crust viscosity to within a factor of about 2. To attempt to constrain η_1, we note that theoretically the

Figure 8

vertical velocity field is very sensitive to the ratio η_c/η_1. A ratio $\gtrsim 3$ is weakly suggested by the vertical χ^2 misfit pattern (Figure 8d). Although the vertical post-seismic signal is greatly contaminated by noise, we believe that this provides a useful constraint on the rheology. The horizontal χ^2 values are lowest for ratios $\eta_c/\eta_1 \lesssim 3$. Together with the vertical misfit patterns this suggests that $\eta_c \sim 3 \times \eta_1$. We thus have a slight preference for a rheology with the following parameters: $\eta_1 = 3 \times 10^{18}$ Pa s, $\eta_2 = 1.0 \times 10^{17}$ Pa s, $\eta_c = 1.0 \times 10^{19}$ Pa s, $\mu_2 = \mu_1 = 70$ GPa. This combination of parameters is indicated by the black circles on the plots of Figure 8.

We compare predicted viscoelastic and observed horizontal velocity fields for the two post-seismic time intervals in Figure 9a-b using this preferred model. Both the pattern and amplitude of elevated post-seismic velocities, particularly the factor of two reduction in velocities between 2000–2001 and 2001–2004, are matched by the viscoelastic model. To assess how well the models fit the data we calculate the weighted RMS residuals as WRMS=$\sqrt{\frac{\chi^2}{N}}$, where χ^2 is calculated from Equation (2), and N is the number of data. Here N=42 stations $\times$ 3 components (=126) for the first year and 53 stations $\times$ 3 components (=159) for the 2001–2004 time interval. The WRMS is 2.0 for the horizontal velocities during the first year and 2.2 for the later time interval. In Figure 9c-d we compare predicted and observed uplift for the preferred low-η_1 model. Due to the large uncertainties in the vertical GPS velocities during the first year the WRMS misfit is 1.2 compared to 1.5 for the 2001–2004 interval, although visually the agreement between the observations and model is better for the latter time interval.

Figure 9

In Figure 10a-b the vertical rates are compared in graphical form for the preferred

Figure 10

low-η_1 model and an alternative high-η_1 model which is also consistent with the horizontal post-seismic velocity pattern (indicated by black triangles in Figure 8). The correlation coefficient between predicted and observed uplift is 0.11 and -0.18 for the low-η_1 and high-η_1 models, respectively.

The choice of mantle rheology and viscosity influences the estimation of η_c. If η_1 were sufficently high ($\eta_1 >> 10^{19}$ Pa s), then mantle flow would be controlled almost entirely by the Kelvin element during the first 4 years. The mantle during times $t << \tau_1$ would then behave as a standard linear solid (SLS), and during the transient period ($t \lesssim \tau_2$) the mantle would gradually relax to a lowered shear modulus of μ' with an exponential decay time of τ_2 (see Equation 2 of *Pollitz* [2003]). Thus the admissible models in Figure 8, near $\eta_1 \sim 5 \times 10^{19}$ Pa s, $\eta_c/\eta_1 = 0.1$, where misfit is low, suggest that inferred crust viscosity is $\eta_c \sim 5 \times 10^{18}$ Pa s for an effectively SLS mantle rheology. For smaller η_1, inferred η_c tends to be larger, *i.e.,* $\eta_c \sim 7 \times 10^{18}$ Pa s for $\eta_1 \sim 10^{19}$ Pa s, and $\eta_c \sim 10^{19}$ Pa s for $\eta_1 \sim 3 \times 10^{18}$ Pa s. In a previous study [*Árnadóttir et al.,* 2003b] we found that inferred η_c is in the range 2–4 $\times 10^{18}$ Pa s and nearly independent of η_1 when a Maxwell rheology is prescribed for the mantle ($\eta_2 = \infty$ and η_1 variable). This shows that the inferred η_c not only depends upon the choice of mantle rheology but also, in the case of a transient rheology, trades off somewhat with mantle viscosity. Note that all transient rheologies considered here have $\eta_1 \leq 10^{20}$ Pa s and thus $\eta_2 \leq 3.6 \times 10^{18}$ Pa s, corresponding to $\tau_2 \leq 1.6$ years. The two candidate models considered in Figure 8 are associated with material relaxation times $\eta_c/\mu_c \sim 10$ yrs in the lower crust and τ_2 = 0.05 yrs or 0.3 yrs and τ_1=1.3 yrs or 8 yrs in the mantle. Thus the observed rapid

decrease in post-seismic velocities between 2000 and 2004 is largely attributed to the influence of mantle relaxation in the viscoelastic models.

7. Afterslip

We now investigate if post-seismic slip (afterslip) on narrow shear zones in the lower crust, below the coseismic ruptures, can provide an alternative mechanism to viscoelastic relaxation. Afterslip has been suggested as an explanation for observed post-seismic deformation in a variety of tectonic settings, *e.g.,* after major strike-slip earthquakes such as the 1999 Izmit, Turkey earthquake [*Reilinger et al.*, 2000; *Bürgmann et al.,* 2002] and following shallow reverse faulting events like the 1999 Chi-Chi, Taiwan earthquake [*Hsu et al.,* 2002]. In addition, deformation transients observed after large subduction earthquakes are usually thought to be caused by afterslip on the subduction interface [e.g. *Heki et al.,* 1997].

Here we estimate afterslip directly from the observed post-seismic GPS data in a similar fashion as co-seismic fault slip is derived. We use fault locations and geometries determined by *Pedersen et al.* [2003] from GPS and InSAR data, extend these faults well into the lower crust and divide them into multiple rectangular sub-faults. We then use the post-seismic GPS data to invert for spatially-variable afterslip during the two time-intervals 2000–2001 and 2001–2004, assuming elastic rheology [*Okada,* 1992]. Following Equation 1, the modeled velocity field at site i for time interval j

$$\mathbf{v}_j(\mathbf{r}_i) = \mathbf{v}_j^{\mathrm{AS}}(\mathbf{r}_i) + \boldsymbol{\Delta}\mathbf{v}_j \tag{3}$$

is the sum of the velocity prediction due to distribution of afterslip $\mathbf{v}_j^{\mathrm{AS}}(\mathbf{r}_i)$ and an estimated velocity shift vector $\boldsymbol{\Delta}\mathbf{v}_j$, as explained in the previous section. We minimize the misfit function in Equation 2 using a non-negative least squares approach, *i.e.,* only allowing for right-lateral afterslip. In addition, we apply smoothing to the solution, but otherwise put no restrictions on where on the fault planes afterslip can take place.

For the 2000–2001 time interval the estimated afterslip is concentrated at depths 8-14 km with a maximum of 40 cm/year on each fault. The afterslip occurs below regions with numerous aftershocks and its distribution appears to be a downward continuation of the co-seismic fault slip as observed in other strike-slip earthquakes (*e.g.,* Izmit 1999 [*Reilinger et al.*, 2000]) (Figure 11). A small amount of shallow afterslip is found near the southern and northern end of the June 21 coseismic rupture which correlates well with the extent of aftershocks. The predicted GPS displacements from this afterslip model explain the main features in the observed GPS displacement field (Figure 9). The weighted RMS for the optimal afterslip model is 1.4 and 1.1 for the horizontal and vertical components, respectively for the first year compared to 1.9 and 1.7 for the horizontal and vertical components, respectively for the later interval.

Figure 11

The optimal distribution of afterslip for the 2001–2004 interval is less convincing. In this case afterslip is found at shallower depths as well as having two clear slip maxima on each fault plane (Figure 11). If afterslip was driven by the rather smooth coseismic fault slip distribution, then multiple afterslip maxima seem unlikely. These afterslip maxima, however, appear to the north and to the south of the afterslip maxima found for the earlier interval in 2000–2001 on both faults. Therefore, one could argue that

afterslip first occurred directly below the coseismic slip and then propagated both to the south and to the north.

8. Discussion

Several previous studies have advocated for afterslip being the main post-seismic mechanism for large ($M_w \sim 7.4$) strike-slip earthquakes [*e.g., Hearn,* 2003], while some other studies have concluded that viscoelastic relaxation is the dominant mechanism [*e.g., Pollitz et al.,* 2001; *Pollitz*, 2003;2005; *Freed and Bürgman*, 2004]. The observed post-seismic deformation in the SISZ does not clearly favor one of these two mechanisms; both seem equally likely. The GPS velocity field shows an overall right-lateral motion and suggests uplift across the whole area (Figure 9). While the horizontal velocity pattern may either be caused by afterslip below the coseismic ruptures or by viscoelastic relaxation, neither mechanism can fully explain the observed vertical velocity field, despite allowing for a vertical shift of about 2–3 mm/yr in the modeling. A direct comparison of the model fits for the viscoelastic and afterslip models is not straightforward, as smoothing and non-negativity constraints in the afterslip modeling reduce the number of independent model parameters significantly. In general one would expect a lower misfit for the afterslip models than the viscoelastic model, since the former many more model parameters; 283 instead of only 5 for the viscoelastic model. The data alone (*i.e.,* a null model) give rise to a WRMS of 2.6 for the first year (2000–2001) and 3.3 for later time interval (2001–2004). The WRMS for the viscoelastic model is 1.8 for the first year compared to 2.0 for the later interval, whereas the weighted

RMS for the optimal afterslip model is 1.3 for the first year, compared to 1.8 for the later interval. The estimated distribution of afterslip appears more plausible during the first year than for the latter time interval. Therefore, we suggest that viscoelastic relaxation and afterslip occurred during the first year, but viscoelastic relaxation was the dominant mechanism during the later years. A more sophisticated model using numerical methods to allow for all three processes (*i.e.,* poro-elastic and viscoelastic relaxation and afterslip) to be active simultaneously during the first year, is outside the scope of our study.

Several studies estimating the rheological properties under Iceland from geodetic data have been published. A range of viscosities from 1×10^{18} to 5×10^{19} Pa s (under a 10 km thick elastic crust) was deduced from lake tilt measurements using a model of glacial rebound due to shrinking of Vatnajökull, Iceland's largest glacier [*Sigmundsson and Einarson,* 1992]. GPS measurements in North Iceland have shown a large continuing rift-normal extension away from the plate boundary, following the Krafla rifting episode that took place in 1975-1984 [*Björnsson,* 1985]. This extension has been interpreted as being predominantly due to post-rifting stress relaxation after the rifting episode. *Heki et al.* [1993] found that displacements observed in N-Iceland from 1987 to 1990 are consistent with a 2D-model of a thin elastic plate over a Newtonian viscous layer with a viscosity $0.3 - 2 \times 10^{18}$ Pa s. A similar value of 1.1×10^{18} Pa s was estimated using GPS data from 1987-1992 and a model consisting of 10 km thick elastic crust overlaying a viscoelastic halfspace [*Hofton and Foulger,* 1996]. *Pollitz and Sacks* [1996] applied a layered viscoelastic model to the same data set and found lower crustal and

upper mantle viscosities of 3×10^{19} Pa s and 3×10^{18} Pa s, respectively. A study of GPS velocities from 1994 to 2003 across the Western and Eastern Volcanic Zones, assuming a Maxwell rheology in a half-space below an elastic plate, suggests viscosities of 4×10^{19} Pa s [*La Femina et al.,* 2005]. Our preferred viscoelastic relaxation model for the SISZ is similar to that of *Pollitz and Sacks* [1996], with lower crustal viscosity of $0.5 - 1 \times 10^{19}$ Pa s and upper mantle viscosity of about 3×10^{18} Pa s.

An outstanding question is whether or not the post-seismic processes after the June 2000 earthquakes have increased the stress on faults in the SISZ. Large earthquakes in the SISZ tend to occur in sequences on several parallel N-S striking faults that are separated by 15-20 km. These sequences typically begin in the east and then progress to the west. As the June 2000 sequence consisted of only two earthquakes, it is important to study stress changes on N-S striking faults located 15-20 km to the west of the June 21 rupture, and also to the east of the June 17 rupture, which are the most likely locations of the next large earthquake. Coseismic Coulomb failure stress (CFS) change calculations indeed show significant positive CFS changes in these areas, indicating that dextral N–S striking faults at these locations were brought closer to failure [*Árnadóttir et al.,* 2003a]. Stress calculations using our preferred afterslip models reveal a similar pattern of CFS changes suggesting that afterslip would further load these faults by $\sim$0.05 MPa. Similarly, our optimal viscoelastic model predicts an overall $\sim 0.02 - 0.06$ MPa CFS increase in the epicentral area with positive changes extending about 20 km to the east and west from the mainshock ruptures. Therefore, both post-seismic mechanisms appear to further load the favorably oriented faults to the west and to the

east of the June 2000 mainshock faults.

The total geodetic moment of the two M=$_w$6.5 June 2000 earthquakes has been estimated $\sim 1 \times 10^{19}$ Nm [*Árnadóttir et al.,* 2001; *Pedersen et al.,* 2003] using $M_0 = \mu A u$, where μ is the shear modulus, A fault area, and u mean slip. *Sigmundsson et al.* [1995] used the rate of geometric moment, $\dot{M}_0/\mu$, as a measure to compare the rate of moment build-up in the SISZ due to plate spreading, estimated as $1.0 - 2.5 \times 10^7$ m^3/yr, to the rate of seismic moment release in historical times, estimated as $2.0 - 2.3 \times 10^7$ m^3/yr [*Stefánsson and Halldórsson,* 1988; *Hackman et al.,* 1990]. The geometric moment of the two June 2000 mainshocks is about 3×10^8 m^3, whereas the moment built up since the M$_S$=7.0 earthquake in 1912 is $9 - 22 \times 10^8$ m^3 [*Pedersen et al.,* 2003]. The June 2000 mainshocks therefore released at most only one-third of the moment built up due to plate spreading in the previous 88 years. Our afterslip model adds about 1×10^8 m^3, over the 4 years that our data spans. We therefore conclude that there is still a significant amount of moment stored in the brittle crust in the SISZ, suggesting that we may expect large earthquakes there in the near future. Our stress change calculations indicate that the areas west of the June 21 rupture and east of the June 17 rupture remain the most likely areas of future earthquakes.

9. Conclusions

Post-seismic deformation observed with GPS in the SISZ after two M$_w$=6.5 earthquakes is modeled using viscoelastic rheology and afterslip. The optimal afterslip models have slip at 8–14 km depth below the coseismic ruptures during the first year

and slip extending further north and south during the succeeding 3 years. The preferred viscoelastic relaxation model has a lower crust viscosity of about 10^{19} Pa s, and poorly constrained mantle viscosity of 3×10^{18} Pa s. This is based on joint consideration of a robust horizontal velocity field and a marginally significant vertical velocity field. Consideration of the horizontal velocity data alone constrains the lower crustal viscosity to the range 0.5–1 $\times$ 10^{19} Pa s. Given the different number of parameters used in the two types of models, it is difficult to favor one model over another on the basis of data fit alone. Both types of post-seismic deformation models suggest that the areas east of the June 17 and west of the June 21 ruptures, that had a large co-seismic stress increase, continue to be loaded by the post-seismic deformation.

Acknowledgments. We are greatful for the invaluable contribution made by the numerous people collecting the vast amount of GPS campaign data used in this study. This work has benefitted from discussions with Halldór Geirsson, Sigrún Hreinsdóttir and Freysteinn Sigmundsson. Comments from Giorgio Spada and two anonymous reviewers helped us improve the text. B. Thorbjarnardóttir at the Icelandic Meteorological Office provided the hypocenter locations shown in Figure 11. This work was supported in part by the Icelandic Research Council grant 031590003, EU contract EVG1-CT-2001-0044 (RETINA), and EU contract EVG1-CT-2002-00073 (PREPARED). The European Space Agency provided the SAR data. Many of the figures were produced using the GMT public domain software [*Wessel and Smith,* 1998].

References

Allen, R. M., G. Nolet, W. J. Morgan, K. Vogfjörd, M. Nettles, G. Ekström, B. H. Bergsson, P. Erlendsson, G. R. Foulger, S. Jakobsdóttir, B. R. Julian, M. Pritchard, S. Ragnarsson, and R. Stefánsson (2002), Plume-driven plumbing and crustal formation in Iceland, *J. Geophys. Res., 107*, doi:10.1029/2001JB000584.

Altamimi, Z., P. Sillard, and C. Boucher (2002), ITRF2000: A new release of the International Terrestrial Reference Frame for Earth science application, *J. Geophys. Res., 107*, 2214, doi:10.1029/2001JB000561.

Árnadóttir, Th., S. Hreinsdóttir, G. Gudmundsson, P. Einarsson, M. Heinert, and C. Völksen (2001), Crustal deformation measured by GPS in the South Iceland Seismic Zone due to two large earthquakes in June 2000, *Geophys. Res. Lett., 28*, 4031–4033.

Árnadóttir, Th., S. Jónsson, R. Pedersen, and G. Gudmundsson (2003a), Coulomb stress changes in the South Iceland Seismic Zone due to two large earthquakes in June 2000, *Geophys. Res. Lett., 30*, doi:10.1029/2002GL016495.

Árnadóttir, Th., F. F. Pollitz, S. Jónsson, K. L. Feigl, E. Sturkell, H. Geirsson, and P. Einarsson (2003b), Spatio-temporal variations of post-seismic deformation after the June 2000 earthquake sequence in southwest Iceland, *Eos Trans. AGU, 84*(46), Fall Meet. Suppl., Abstract G21B-0268.

Árnadóttir, Th., H. Geirsson, and P. Einarsson (2004), Co-seismic stress changes and crustal deformation on the Reykjanes Peninsula due to triggered earthquakes on June 17, 2000 *J. Geophys. Res., 109*, B09307, doi:10.1029/2004JB003130.

Árnadóttir, Th., W. Jiang, K. L. Feigl, H. Geirsson, and E. Sturkell (2005), Kinematic models

of plate boundary deformation in southwest Iceland derived from GPS observations, *J. Geophys. Res.,* doi:10.1029/2005JB003907.

Bills, B. G., D. R. Currey, and G. A. Marshall (1994), Viscosity estimates for the crust and upper mantle from patterns of lacustrine shoreline deformation in the Eastern Great Basin, *J. Geophys. Res., 99*, 22,059-22,086.

Bjarnason, I., P. Cowie, M. H. Anders, L. Seeber, and C. H. Scholz (1993a), The 1912 Iceland earthquake rupture: Growth and development of a nascent transform system, *Bull. Seismol. Soc. Am., 83*, 416–435.

Bjarnason, I. Th. W. Menke, Ó. G. Flóvenz, and D. Caress (1993b), Tomographic image of the mid-Atlantic plate boundary in southwestern Iceland, *J. Geophys. Res., 98*(B4), 6607-6622.

Björnsson, A., (1985), Dynamics of crustal rifting in Iceland, *J. Geophys. Res., 90*, 10,151-10,162.

Björnsson, G., Ó. G. Flovenz, K. Sæmundsson, and E. H. Einarsson (2001), Pressure changes in Icelandic geothermal reservoirs associated with two large earthquakes in June 2000, *Proc. 26th Workshop on Geothermal Reservoir Engineering*, SGP-TR_168, 327–334, Stanford University, Stanford, CA, USA.

Bürgmann, R., S. Ergintav, P. Segall, E. H. Hearn, S. McClusky, R. E. Reilinger, H. Woith, and J. Zschau (2002), Time-space variable afterslip on and deep below the Izmit earthquake rupture, *Bull. Seismol. Soc. Am., 92*, 126–137.

Dziewonski, A. M., G. Ekstrom, and N. N. Maternovskaya (2001), Centroid-moment tensor solutions for April-June 2000, *Phys. Earth Planet. Inter., 123*, 1–14.

Clifton, A. E., C. Pagli, J. F. Jónsdóttir, K. Eythórsdóttir and K. Vogfjörd (2003), Surface effects of triggered fault slip on Reykjanes Peninsula, SW Iceland, *Tectonophysics, 369*, 145–154.

Clifton, A.E., and P. Einarsson (2005), Styles of surface rupture analysis accompanying the June 17 and 21, 2000 earthquakes in the South Iceland Seismic Zone, *Tectonophysics, 396*, 141–159.

Einarsson, P. , and J. Eiríksson (1982), Earthquake fractures in the districts Land and Rangárvellir in the South Iceland Seismic Zone, *Jökull, 32*, 113–120.

Einarsson, P., S. Björnsson, G. Foulger, R. Stefánsson, and Th. Skaftadóttir (1981), Seismicity pattern in the South Iceland Seismic Zone, in *Earthquake Prediction – An international review*, D. W. Simpson and P. G. Richards (editors), AGU, vol. 4, 141–151.

Feigl, K. L., J. Gasperi, F. Sigmundsson, and A. Rigo (2000), Crustal deformation near Hengill volcano, Iceland 1993–1998: Coupling between magmatic activity and faulting inferred from elastic modeling of satellite radar interferograms, *J. Geophys. Res., 105*, 25,655–25,670.

Freed A., and R. Bürgman (2004), Evidence of powerlaw flow in the Mojave desert mantle, *Nature, 430*, 548–551.

Hackman, M. C., G. C. P. King, and R. Bilham (1990), The mechanics of the south Iceland seismic zone, *J. Geophys. Res., 95*, 17,339–17,351.

Hearn, E. H. (2003), What can GPS data tell us about the dynamics of post-seismic deformation? *Geophys. J. Int., 155*, 753–777.

Heki, K., G. R. Foulger, B. R. Julian, and C.-H. Jahn (1993), Plate dynamics near divergent

boundaries: Geophysical implications of postrifting crustal deformation in NE Iceland, *J. Geophys. Res., 98*(B8), 14,279-14,298.

Heki, K., S. Miyazaki, and H. Tsuji (1997), Silent fault slip following an interplate thrust earthquake at the Japan trench, *Nature, 386,* 595–598.

Herring, T. A. (2003), *GLOBK: Global Kalman filter VLBI and GPS analysis program*, version 4.1, Mass. Inst. Technol., Cambridge, MA, USA.

Hofton, M. A., and G. R. Foulger (1996), Postrifting anelastic deformation around the spreading plate boundary, north Iceland 1. Modeling of the 1987–1992 deformation field using a viscoelastic Earth structure, *J. Geophys. Res., 101*(B11), 25,403-25,422, doi:10.1029/96JB02466.

Hsu, Y.-J., N. Bechor, P. Segall, S.-B. Yu, L.-C. Kuo, and K.-F. Ma (2002), Rapid afterslip following the 1999 Chi-Chi, Taiwan Earthquake, *Geophys. Res. Lett., 29*, doi:10.1029/2002GL014967.

Ivins , E. R. (1996), Transient creep of a composite lower crust, 2. A polymineralic basis for rapidly evolving postseismic deformation modes, *J. Geophys. Res., 101*, 28,005–28,028.

Jónsson, S., P. Segall, R. Pedersen, and G. Björnsson (2003), Post-earthquake ground movements correlated to pore-pressure transients, *Nature, 424*, 179–183.

King, R. W., and Y. Bock (2003), *Documentation for the GAMIT Analysis Software*, release 10.1, Mass. Inst. Technol., Cambridge, MA, USA.

La Femina, P. C., T. H. Dixon, R. Malservisi, Th. Árnadóttir, E. Sturkell, F. Sigmundsson, and P. Einarsson (2005), Geodetic GPS measurements in south Iceland: Strain

accumulation and partitioning in a propagating ridge system *J. Geophys. Res.,* doi:10.1029/2005JB003675.

McClusky, S., *et al.* (2000), Global Positioning System constraints on plate kinematics and dynamics in the eastern Mediterranean and Caucasus, *J. Geophys. Res., 105*, 5695-5720.

Minster, J. B., and D. L. Anderson (1981), A model of dislocation controlled rheology for the mantle, *Philos. Trans. R. Soc. London, 299*, 319–356.

Okada, Y. (1992), Internal deformation due to shear and tensile faults in a half-space, *Bull. Seism. Soc. Am., 82,* 1018–1040.

Pagli, C., R. Pedersen, F. Sigmundsson, and K. L. Feigl (2003), Triggered seismicity on June 17, 2000 on Reykjanes Peninsula, SW-Iceland captured by radar interferometry, *Geophys. Res. Lett., 30*(6), 1273, doi:10.1029/2002GL015310.

Pedersen, R., F. Sigmundsson, K. L. Feigl, and Th. Árnadóttir (2001), Coseismic interferograms of two M_S=6.6 earthquakes in the South Iceland Seismic Zone, June 2000, *Geophys. Res. Lett., 28*, 3341–3344.

Pedersen, R., S. Jónsson, Th. Árnadóttir, F. Sigmundsson, and K. L. Feigl (2003), Fault slip distribution of two M_w=6.5 earthquakes in South Iceland estimated from joint inversion of InSAR and GPS measurements, *Earth and Planet. Sci. Lett., 213*, 487–502.

Peltier, W. R., P. Wu, and D. A. Yuen (1981), The viscosities of the Earth's mantle, in: *Anelasticity in the Earth*, F. D. Stacey, M. S. Paterson, and A. Nicholas (eds), AGU Geodynamics Series, 4, AGU, Washington, 59–77.

Pollitz, F. F., and I. S. Sacks (1996), Viscosity structure beneath northeast Iceland, *J. Geophys. Res., 101*, 17,771–17,793.

Pollitz, F. F. (1997), Gravitational-viscoelastic postseismic relaxation on a layered spherical Earth, *J. Geophys. Res., 102*, 17,921–17,941.

Pollitz, F. F., C. Wicks, W. Thatcher (2001), Mantle flow beneath a continental strike-slip fault: Postseismic deformation after the 1999 Hector Mine earthquake, *Science, 293,* 1814–1818.

Pollitz, F. F. (2003), Transient rheology of the uppermost mantle beneath the Mojave Desert, California, *Earth Planet. Sci. Lett., 215*, 89–104,

Pollitz, F. F. (2005), Transient rheology of the upper mantle beneath central Alaska inferred from the crustal velocity field following the 2002 Denali earthquake, *J. Geophys. Res.,* doi:10.1029/2005JB003676.

Reilinger, R. E., S. Ergintav, R. Bürgmann, S. McClusky, O. Lenk, A. Barka, O. Gurkan, E. Hearn, K. L. Feigl, R. Cakmak, B. Aktug, H. Ozener, and M. N. Toksoz, (2000), Coseismic and postseismic fault slip for the 17 August 1999, M=7.5, Izmit, Turkey earthquake, *Science, 289*, 1519–1524.

Sigmundsson, F., and P. Einarsson (1992), Glacio-isostatic crustal movements caused by historical volume change of the Vatnajökull ice cap, Iceland, *Geophys. Res. Lett., 19*(21), 2123–2126, doi:10.1029/92GL02209.

Sigmundsson, F., P. Einarsson, R. Bilham, and E. Sturkell (1995), Rift-transform kinematics in south Iceland: Deformation from Global Positioning System measurements, 1986 and 1992, *J. Geophys. Res., 100*, 6235–6248.

Sigmundsson, F., P. Einarsson, S. Th. Rögnvaldsson, G. R. Foulger, K. M. Hodgkinsson, and G. Thorbergsson (1997), The 1994–1995 seismicity and deformation at the Hengill

triple junction, Iceland: Triggering of earthquakes by minor magma injection in a zone of horizontal shear stress, *J. Geophys. Res., 102*, 15,151–15,161.

Stefánsson, R., and P. Halldórsson (1988), Strain release and strain build-up in the south Iceland seismic zone, *Tectonophysics, 152*, 267–276.

Stefánsson, R., R. Bödvarsson, R. Slunga, P. Einarsson, S. Jakobsdóttir, H. Bungum, S. Gregersen, J. Havskov, J. Hjelme, and H. Korhonen (1993), Earthquake prediction research in the South Iceland Seismic Zone and the SIL project, *Bull. Seismol. Soc. Am.,* 83, 696–716.

Stefánsson, R., G. Gudmundsson, and P. Halldórsson (2003), The South Iceland earthquakes 2000 - a challenge for earthquake prediction research, report *VI-R03017*, 21 pp, Icelandic Meteorological Office, Reykjavík, Iceland.

Tryggvason, A., S. Th. Rögnvaldsson, and Ó Flóvenz (2002), Three dimensional imaging of the P- and S-wave velocity structure and earthquake locations beneath southwest Iceland, *Geophys. J. Int.*, *151*, 848–866.

Yuen, D. A., R. Sabadini, P. Gasperini, and E. Boschi (1986), On transient rheology and glacial isostasy, *J. Geophys. Res., 91*, 11420–11438.

Wessel, P., and W. H. F. Smith (1998), New, improved version of generic mapping tools released, *Eos Trans. AGU, 79*, 47, 579.

Th. Árnadóttir, Nordic Volcanological Center, Askja, Natural Sciences Building, University of Iceland, IS-101 Reykjavík, Iceland (thora1@hi.is)

K. L. Feigl, Department of Terrestrial and Planetary Dynamics, CNRS-UPS, Observatoire Midi-Pyrenees, 31400 Toulouse, FRANCE. (feigl@pontos.cst.cnes.fr)

W. Jiang, Nordic Volcanological Center, Askja, Natural Sciences Building, University of Iceland, IS-101 Reykjavík, Iceland Now at: GPS Research Center, Wuhan University 129 Luoyu Road, Wuhan 430079, China (wpjiang@whu.edu.cn)

S. Jónsson, Institute of Geophysics, ETH Hoenggerberg, CH-8093 Zurich, Switzerland (sj@erdw.ethz.ch)

F. F. Pollitz, US Geological Survey, Middlefield Rd., Menlo Park, CA (fpollitz@usgs.gov)

Received _____

[1]Nordic Volcanological Center, Institute for Earth Sciences, University of Iceland, Reykjavík, Iceland.

[2]Institute of Geophysics, ETH, Zurich, Switzerland

[3]US Geological Survey, Menlo Park, California, USA

[4]CNRS, Toulouse, France

Submitted to *Journal of Geophysical Research*, February 21, 2005.

Figure 1. Map of the main tectonic features of southwest Iceland. The epicenters of the June 17 and June 21, 2000, earthquakes are shown with large black stars and the four largest aftershocks on June 17 are noted with small gray stars. The locations of the June 17 and 21 fault models are marked by bold gray lines. The locations of the South Iceland Seismic Zone (SISZ), Western Volcanic Zone (WVZ), and the Eastern Volcanic Zone (EVZ) are also shown. Light shaded areas are individual spreading segments with associated central volcanoes. The dashed box outlines the study area. The locations of the campaign GPS stations are denoted with black triangles while the continous GPS stations are shown with black squares. The inset shows the plate-boundary across Iceland and the NUVEL-1A plate motion. The location of Figure 1 is indicated by a box.

Figure 2. Interseismic plate velocities (black arrows with 68% confidence ellipses), relative to REYK (see Figure 1), calculated from GPS campaign observations from 1992 to 1999. Velocities of two CGPS stations (HVER and OLKE) were obtained from data spanning early 1999 – June 2000. High velocities in the vicinity of the Hengill volcano are due to an inflation episode from 1993 to 1998. The white arrows show velocities predicted by a point source model of inflation at Hengill (shown with hexagon) from 1993 to 1998 [*Feigl et al.*, 2000].

Figure 3. Horizontal GPS velocities during the first year (2000–2001) (black arrows with 68% confidence ellipses) in comparison to estimated interseismic plate velocities (white arrows). All velocities are shown relative to REYK.

Figure 4. Post-seismic GPS station velocities (black arrows with 68% confidence ellipses) corrected for interseismic plate motion. (a) Horizontal velocity field for 2000–2001. Motion predicted by a model of poro-elastic relaxation is shown with white arrows [*Jónsson et al.*, 2003]. (b) Horizontal velocity field for 2001–2004. (c) Vertical velocities (in ITRF2000) for 2000–2001, with poro-elastic model prediction (white arrows). (d) Vertical velocities (in ITRF2000) for 2001–2004.

Figure 5. (a) Synthetic aperture radar interferogram (InSAR) showing near vertical post-seismic displacements in the line of sight (LOS) towards the satellite near the June 17 rupture from 19 June to 24 July, 2000. (b) Simulated interferogram assuming poro-elastic relaxation. (c) Average LOS displacement in an E–W profile for interferogram shown in (a), drawn with the red curve, and the model prediction in (b) with blue. After Figure 2 in *Jónsson et al.* [2003].

Figure 6. A transient rheology as represented by a Burgers body. It consists of a Maxwell element in series with a Kelvin element, which are characterized by steady state shear and bulk moduli μ_1 and κ_1, respectively, steady state viscosity η_1, transient viscosity η_2, and transient shear modulus μ_2. If $\eta_1 = \infty$, then the material behaves like a standard linear solid with relaxed shear modulus $\mu' = \mu_1\mu_2/(\mu_1 + \mu_2)$. If $\eta_2 = \infty$ or $\mu_2 = \infty$, then the material behavior reduces to a Maxwell rheology.

Figure 7. Layerd Earth model for the SISZ used in this study. We assume an elastic upper crust down to 10 km, based on average depth of earthquake hypocenters in the SISZ, and a lower crust from 10–20 km consistent with seismic studies. Based on similar studies [*Pollitz*, 2003; *Pollitz*, 2005] we assume a Maxwell and Burgers body rheology for the lower crust and upper mantle, respectively. In order to reduce the number of unknowns we adopt scalings among these parameters determined by *Pollitz* [2003] for the upper mantle beneath the Mojave Desert, *i.e.,* values of the ratio μ_2/μ_1 and ratio η_2/η_1.

Figure 8. Residual misfit of a set of viscoelastic models with respect to observed velocities in two time intervals. This is calculated from Equation 2 for the horizontal velocity components (a and b) and for the vertical velocity components (c and d). Black circles and triangles indicate the preferred low-η_1 model and an alternative high-η_1 model.

Figure 9. Observed (blue arrows with 68% confidence ellipses) and calculated velocity fields for the preferred viscoelastic model (black circles in Figure 8), shown with red vectors. The velocities predicted by the best fit afterslip models (Figure 11) are shown with green vectors. The bold gray lines denote the up-dip surface projection of the afterslip fault models. The horizontal velocity field for (a) the 2000–2001 interval, (b) the 2001–2004 interval. The vertical velocity field for (c) 2000–2001, (d) 2001–2004. The model velocity fields have been corrected for the estimated shift of $\mathbf{\Delta v}$ (Equation 1), which is approximately 1–2 mm/yr in horizontal and 2–3 mm/yr in vertical.

Figure 10. Graphical comparison of observed and calculated velocity fields for the 2001–2004 interval for the preferred low-η_1 model (black circles in Figure 8) and the alternative high-η_1 model (black triangles in Figure 8). In each case the model velocity values have been corrected for the vertical component of $\mathbf{\Delta v}$ (Equation 1), which is approximately 3 mm/yr. The correlation coefficient is 0.11 and -0.18 for the low-η_1 and high-η_1 models, respectively.

Figure 11. Distributed slip models for the (a) June 17 rupture and (b) June 21 rupture. Afterslip models for the different intervals (2000–2001 and 2001–2004) are shown in the top middle and right panels respectively. The coseismic slip distribution is shown in the top left panel. The lower three panels show the cumulative slip for the different time intervals, *i.e.,* coseismic and first year of post-seismic slip (left), coseismic and first four years of post-seismic slip (middle) and total afterslip (right). The black dots are earthquake hypocenters recorded by the SIL seismic network during the two time intervals (B. Thorbjarnardóttir, pers. communication, 2004).

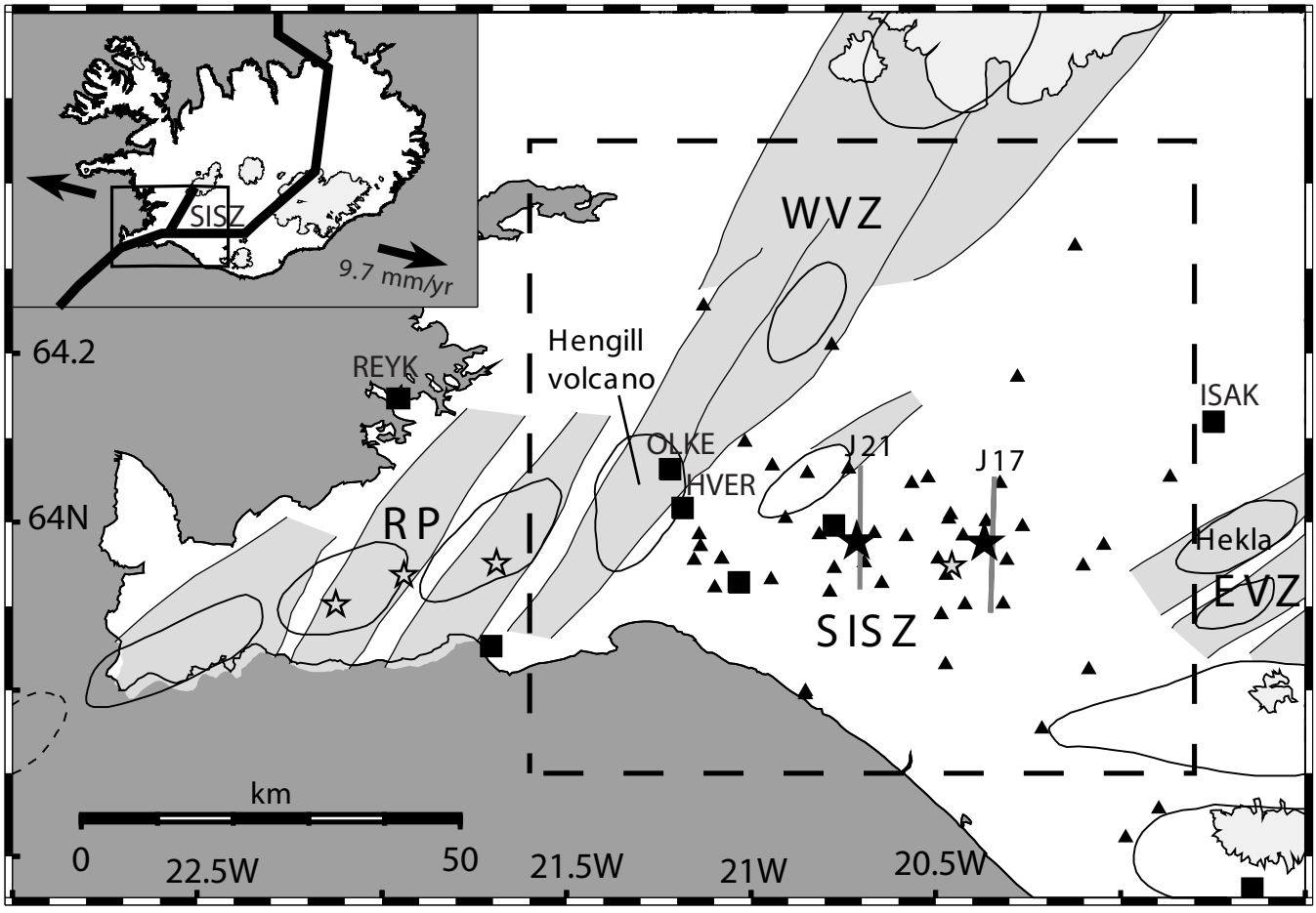

Árnadóttir et al, Figure 1

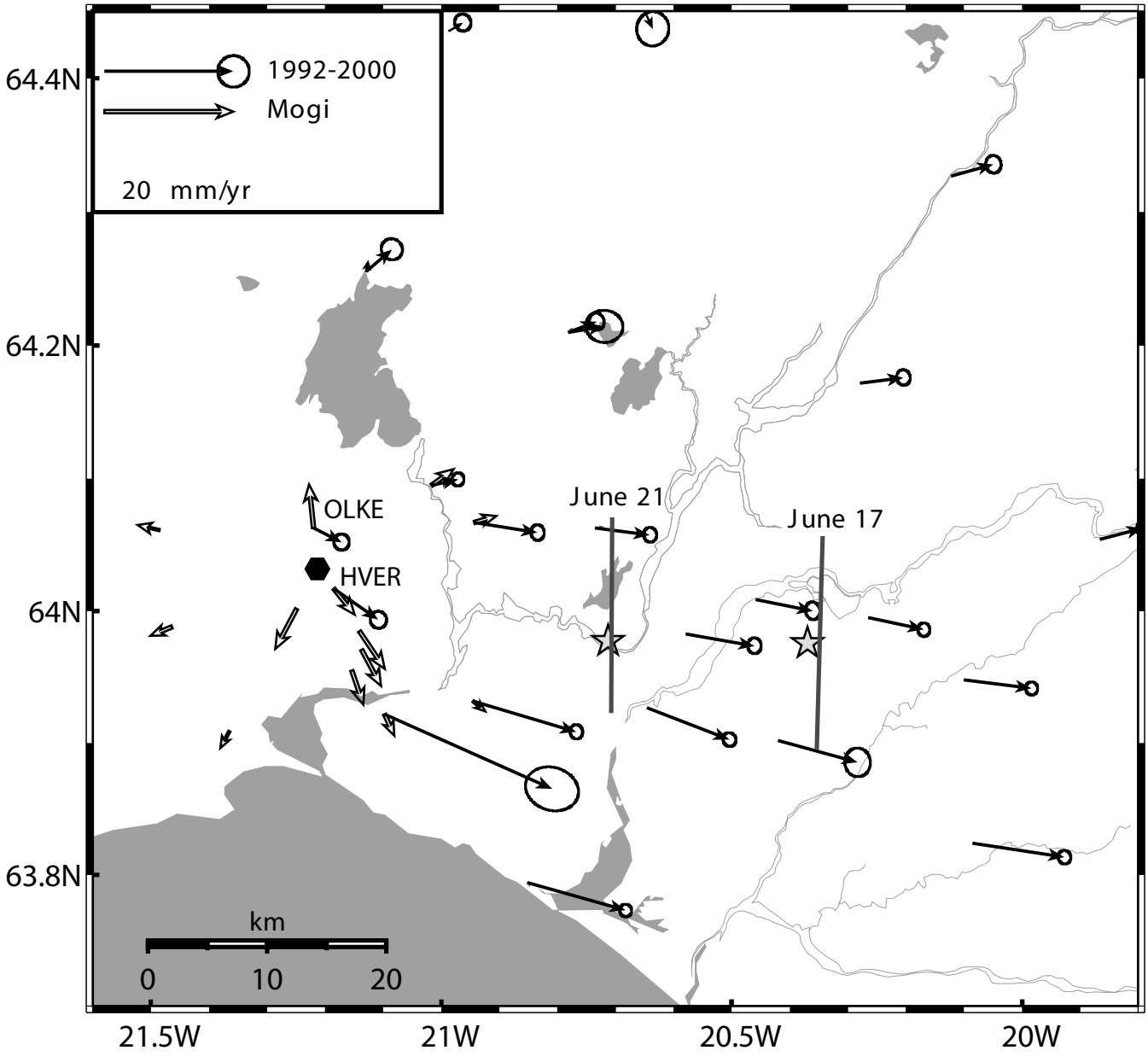

Árnadóttir et al, Figure 2

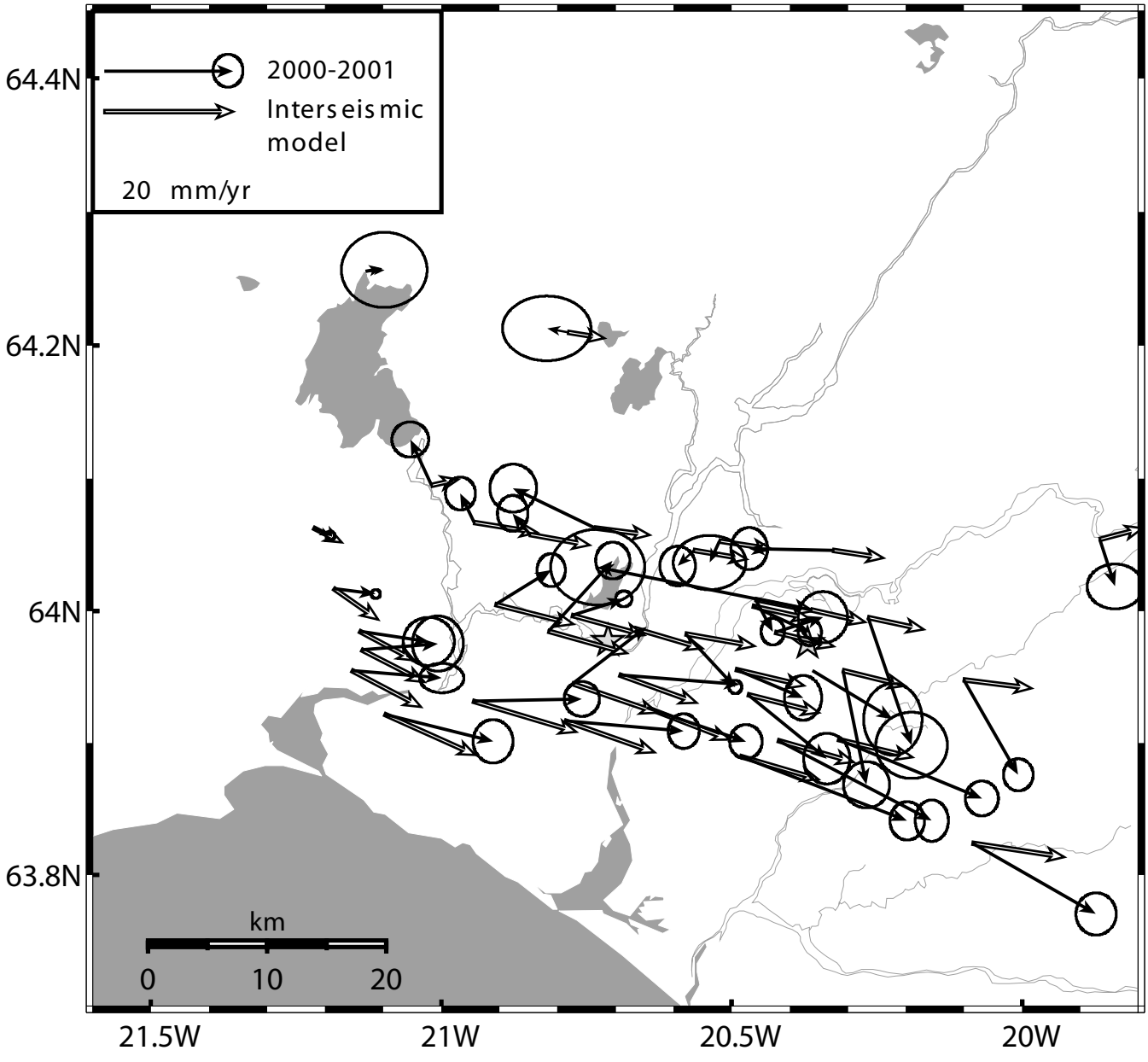

Árnadóttir et al., Figure 3

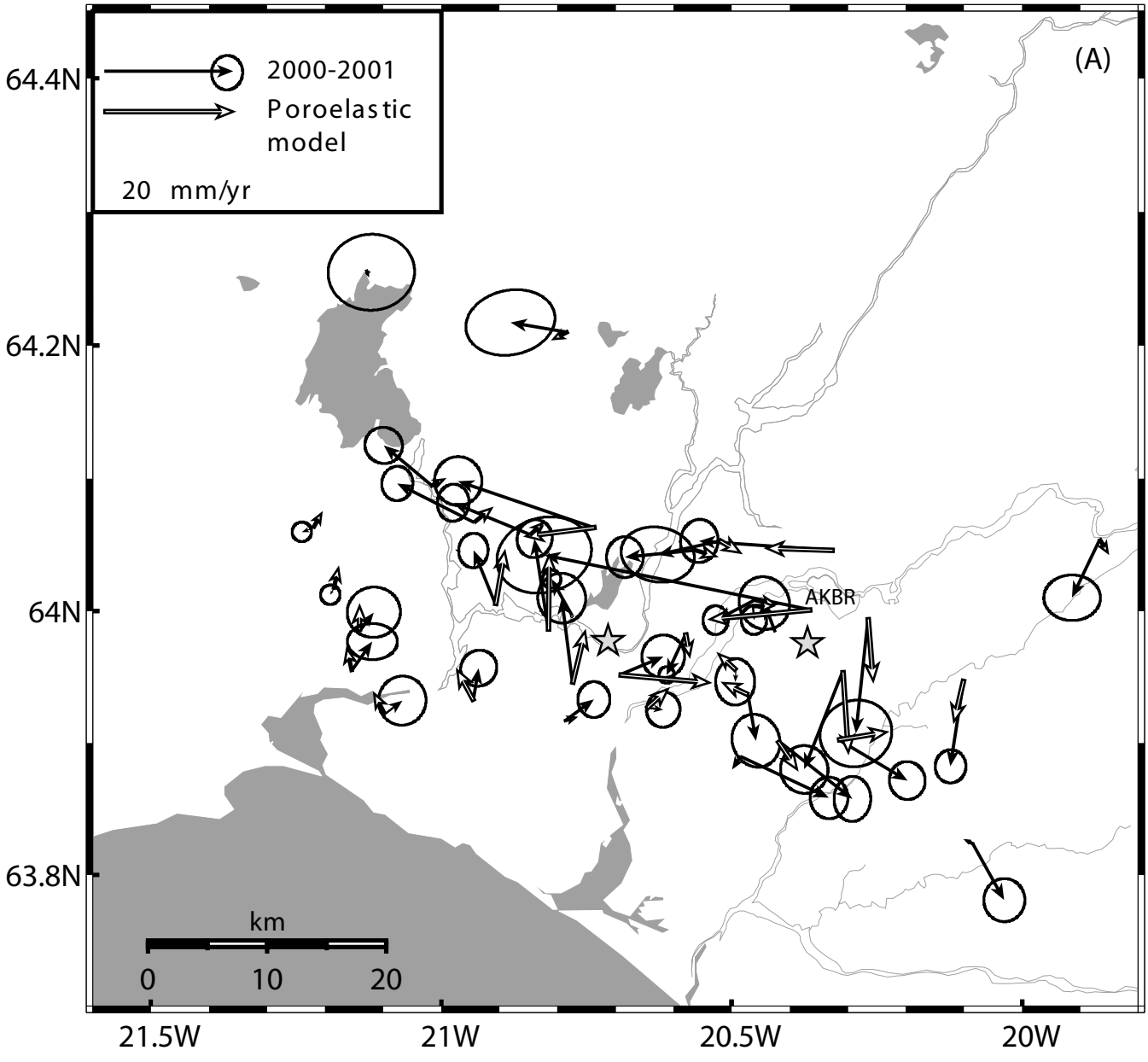

Árnadóttir et al., Figure 4a

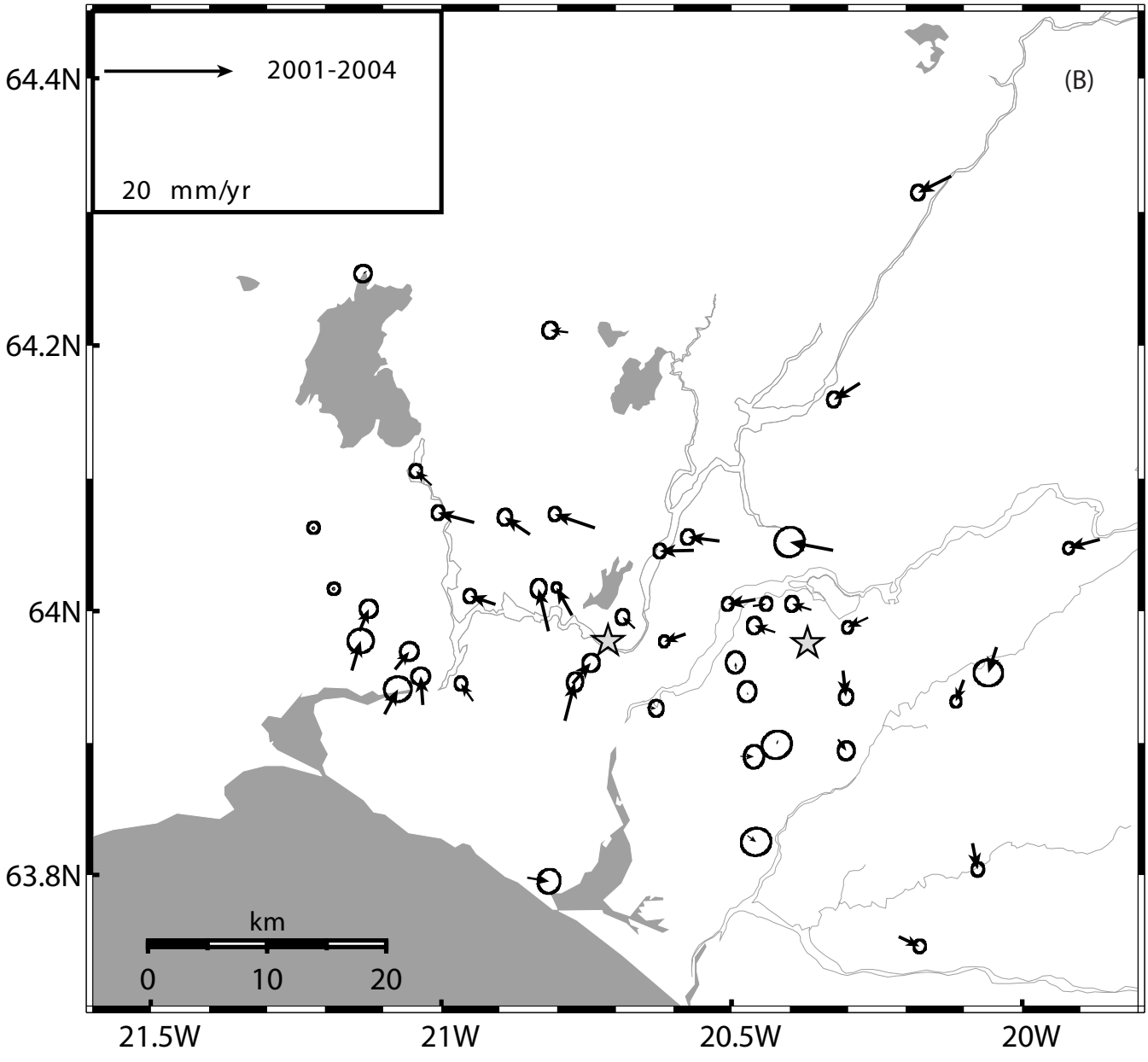

Árnadóttir et al, Figure 4b

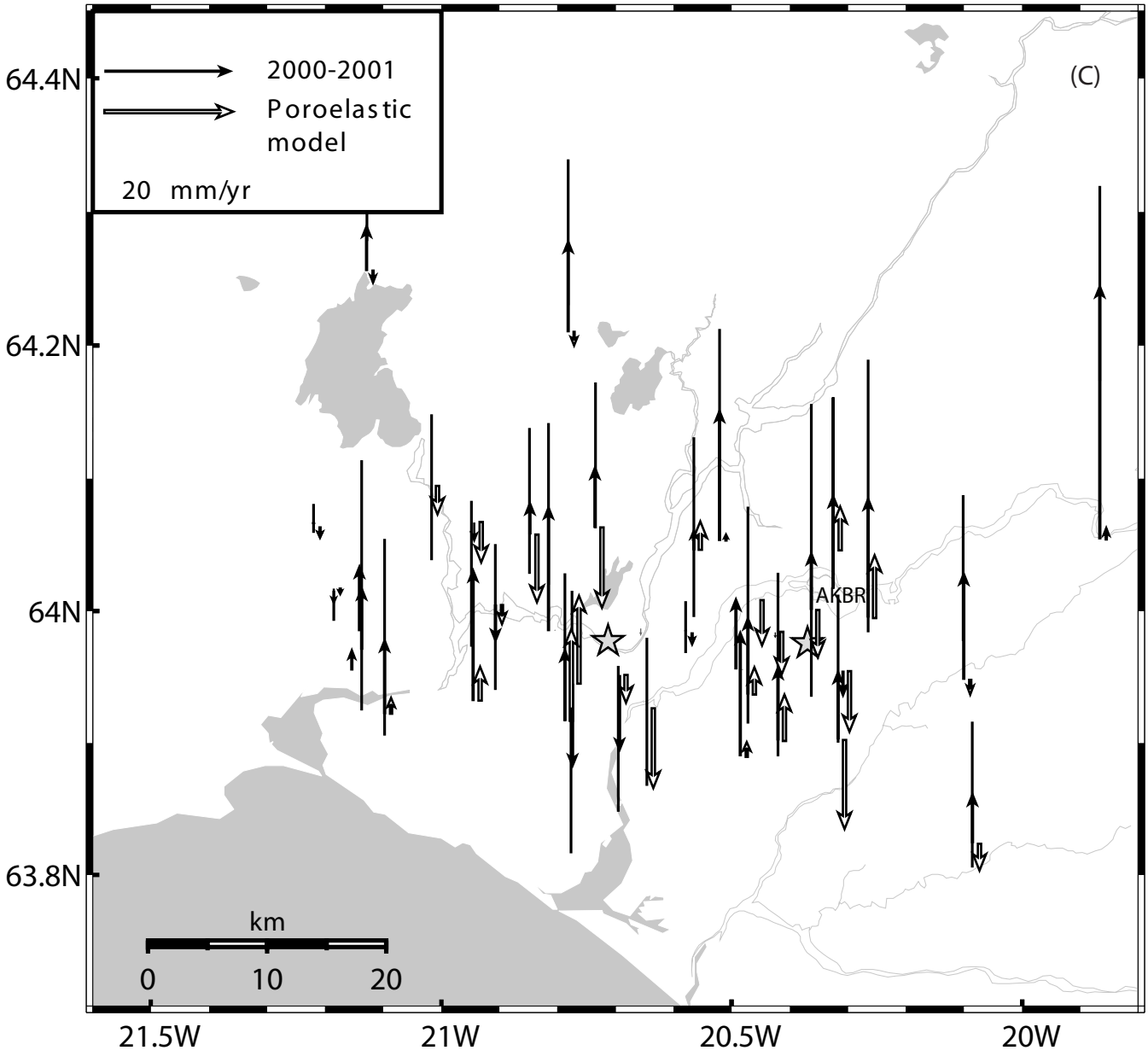

Árnadóttir et al, Figure 4c

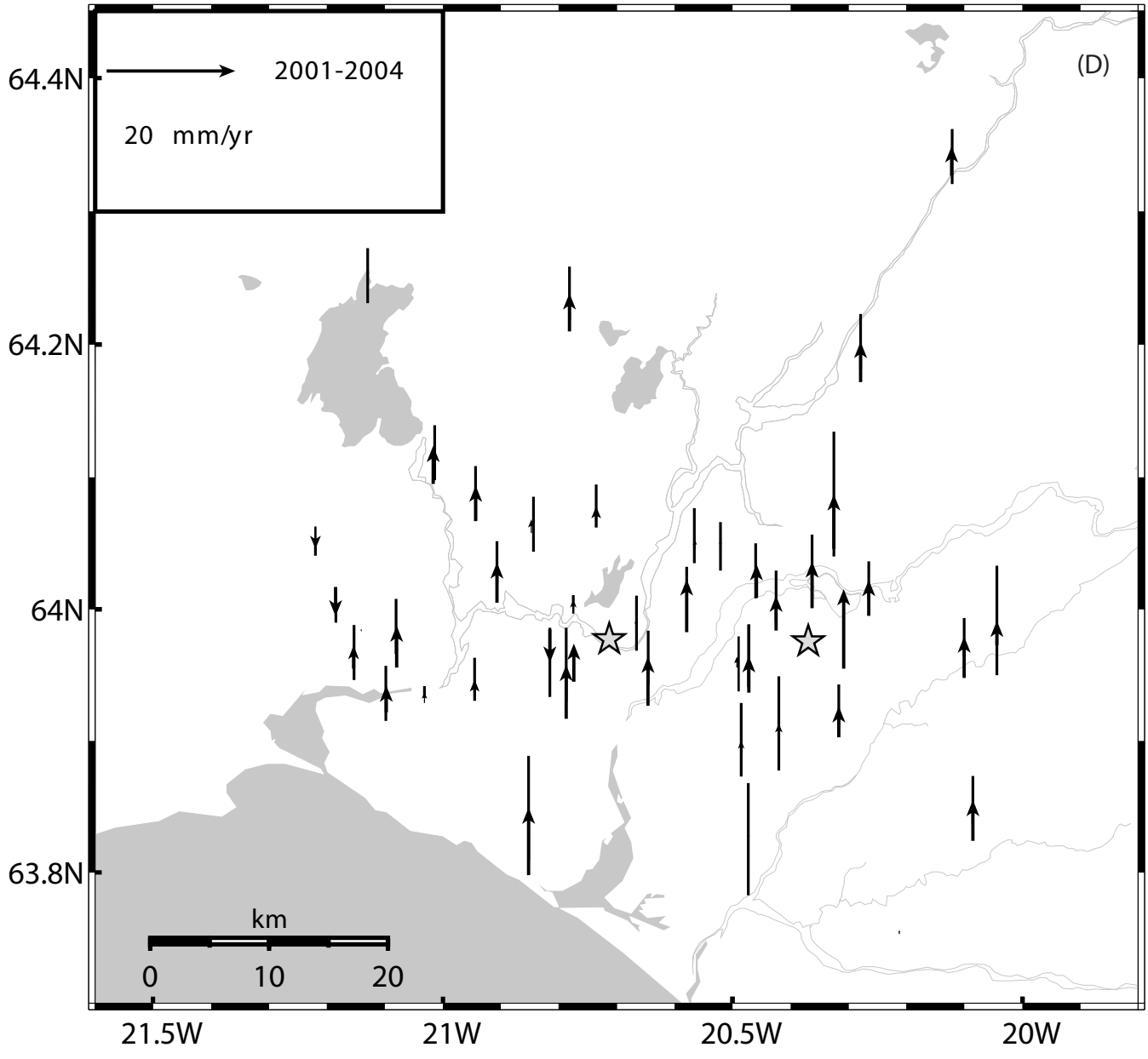

Árnadóttir et al, Figure 4d

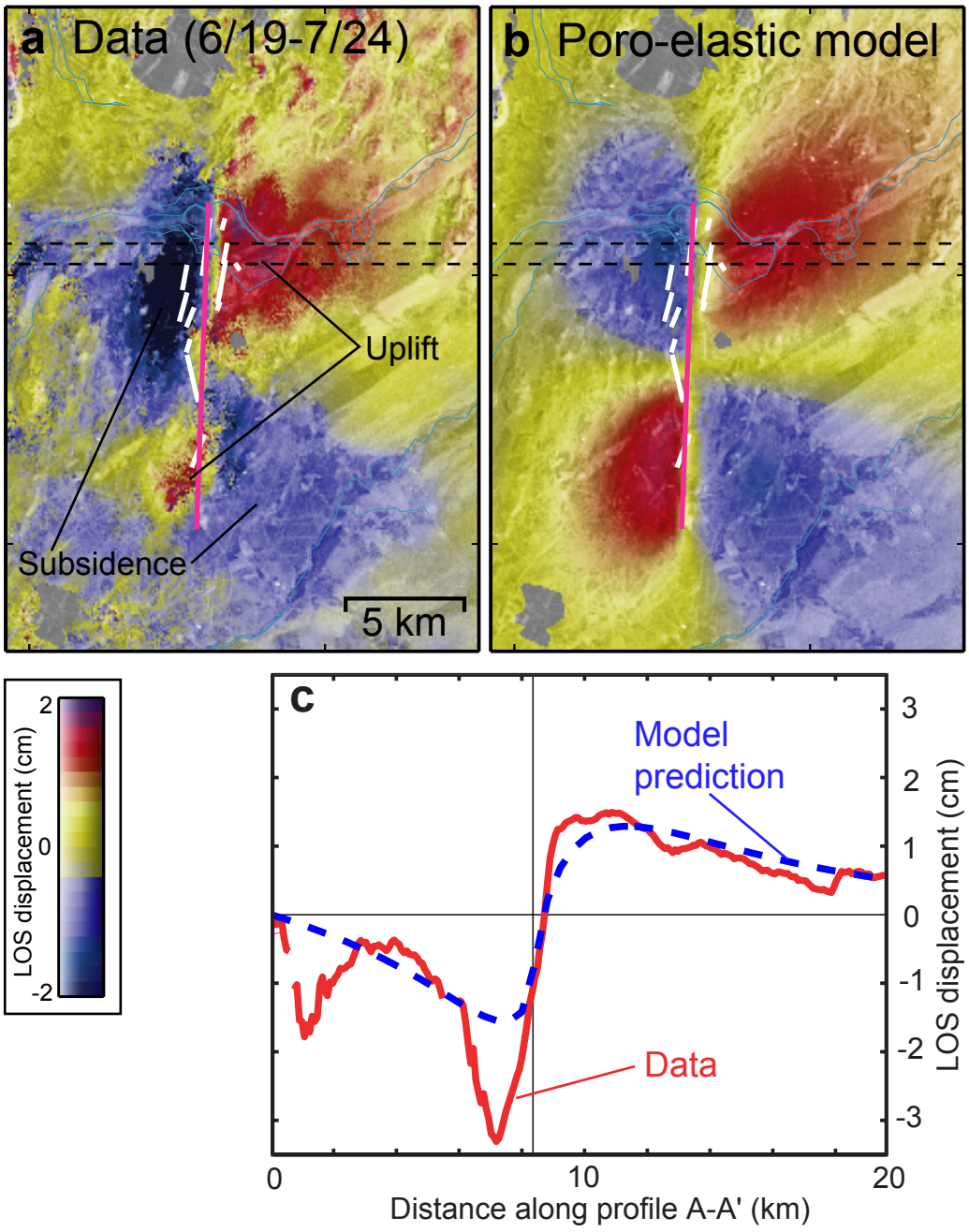

Árnadóttir et al., Figure 5

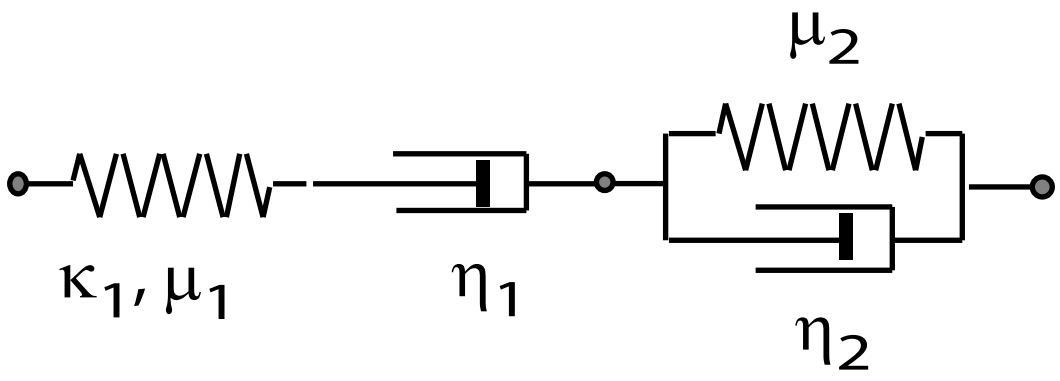

Árnadóttir et al, Figure 6

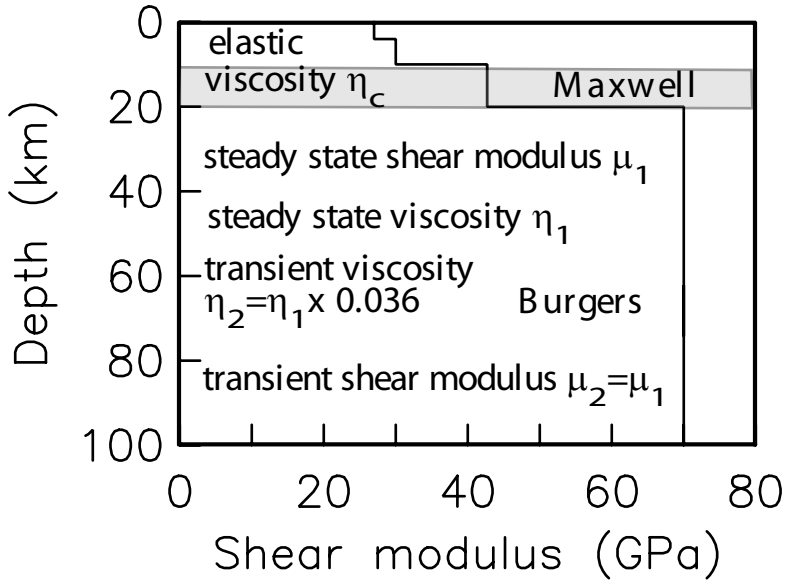

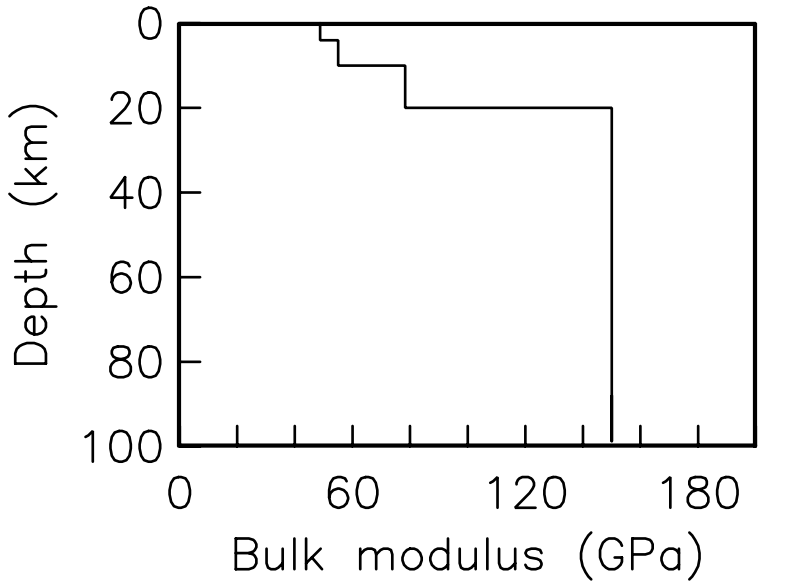

Árnadóttir et al, Figure 7

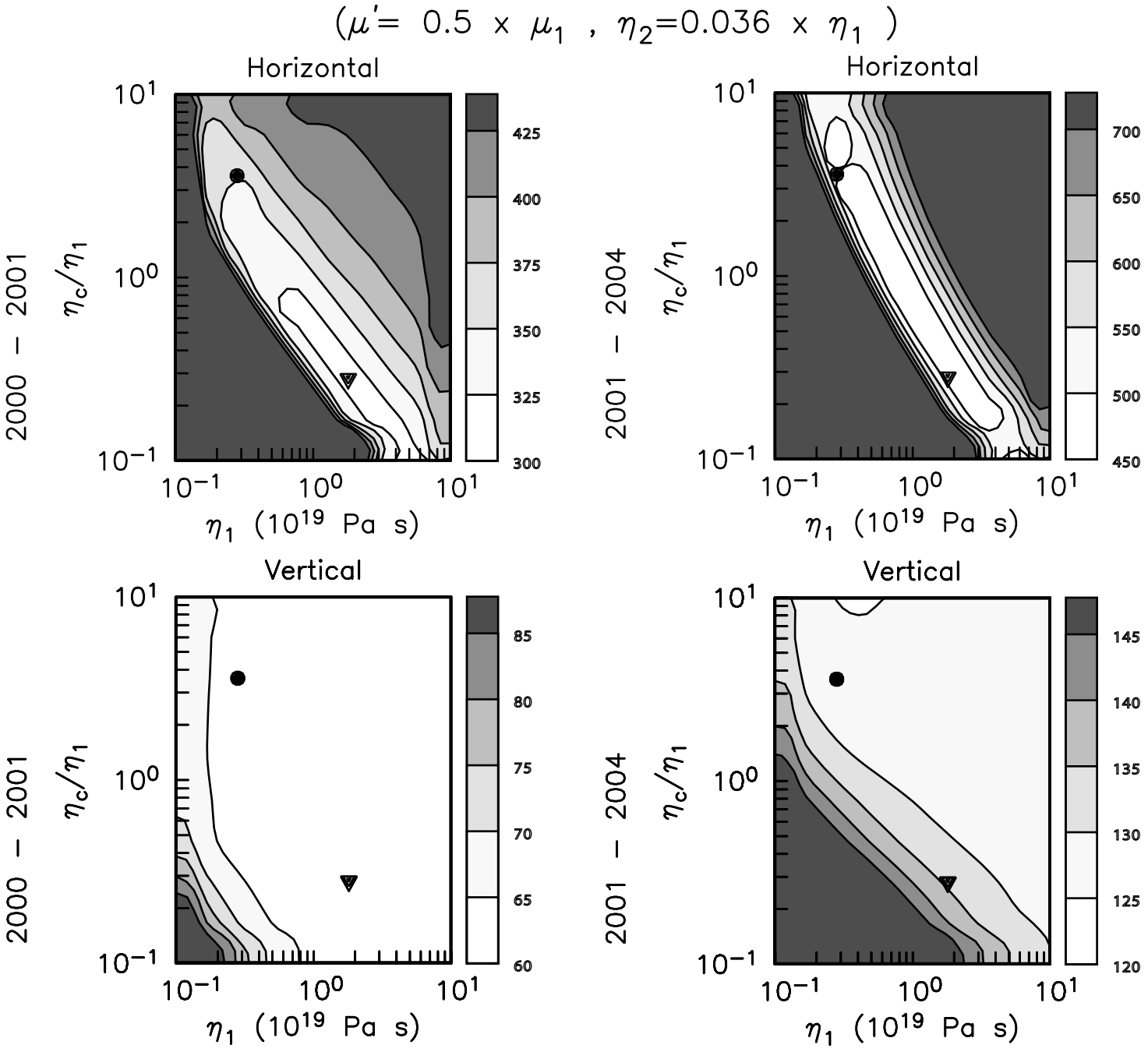

Árnadóttir et al, Figure 8

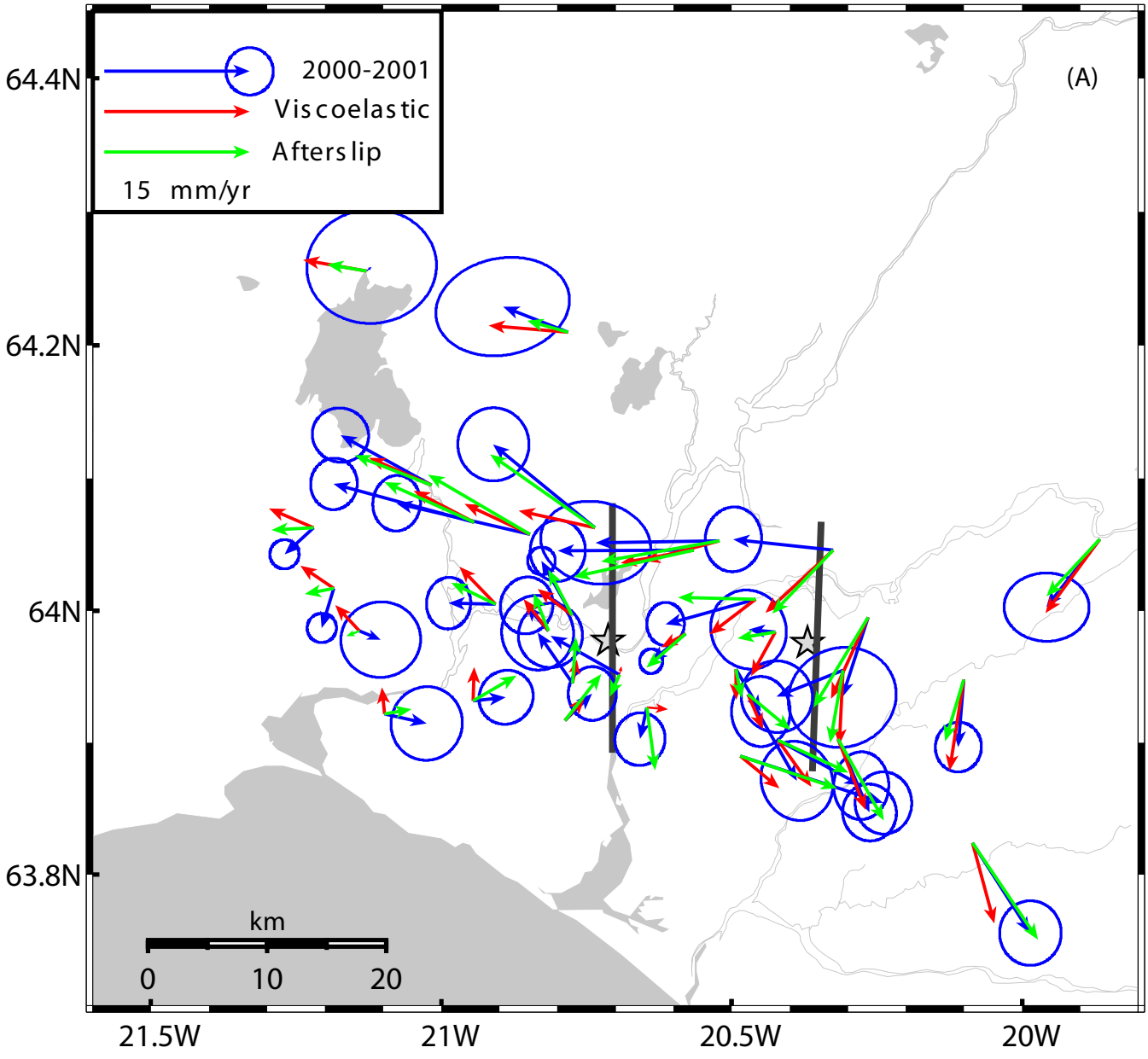

Árnadóttir et al, Figure 9a

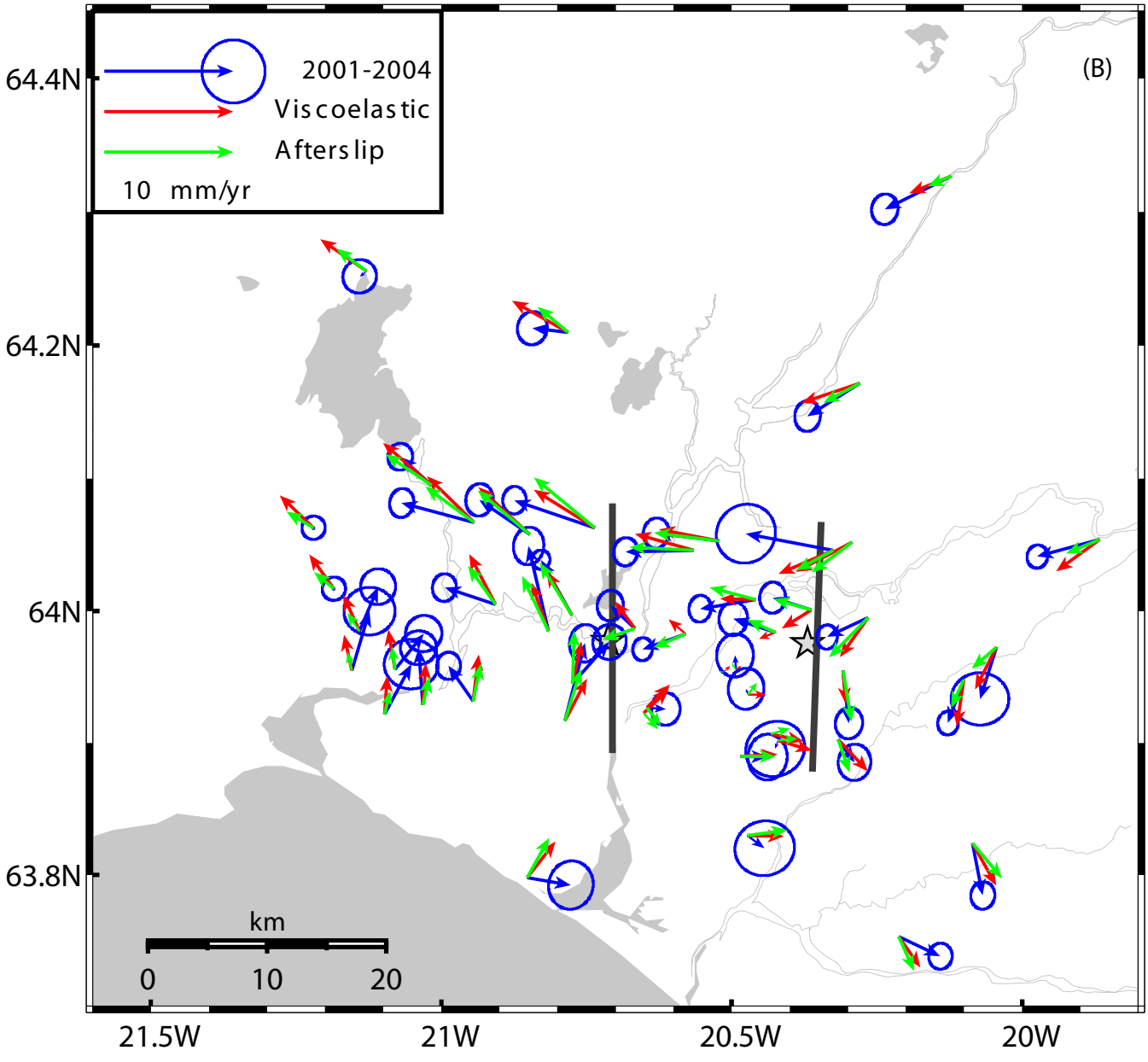

Árnadóttir et al, Figure 9b

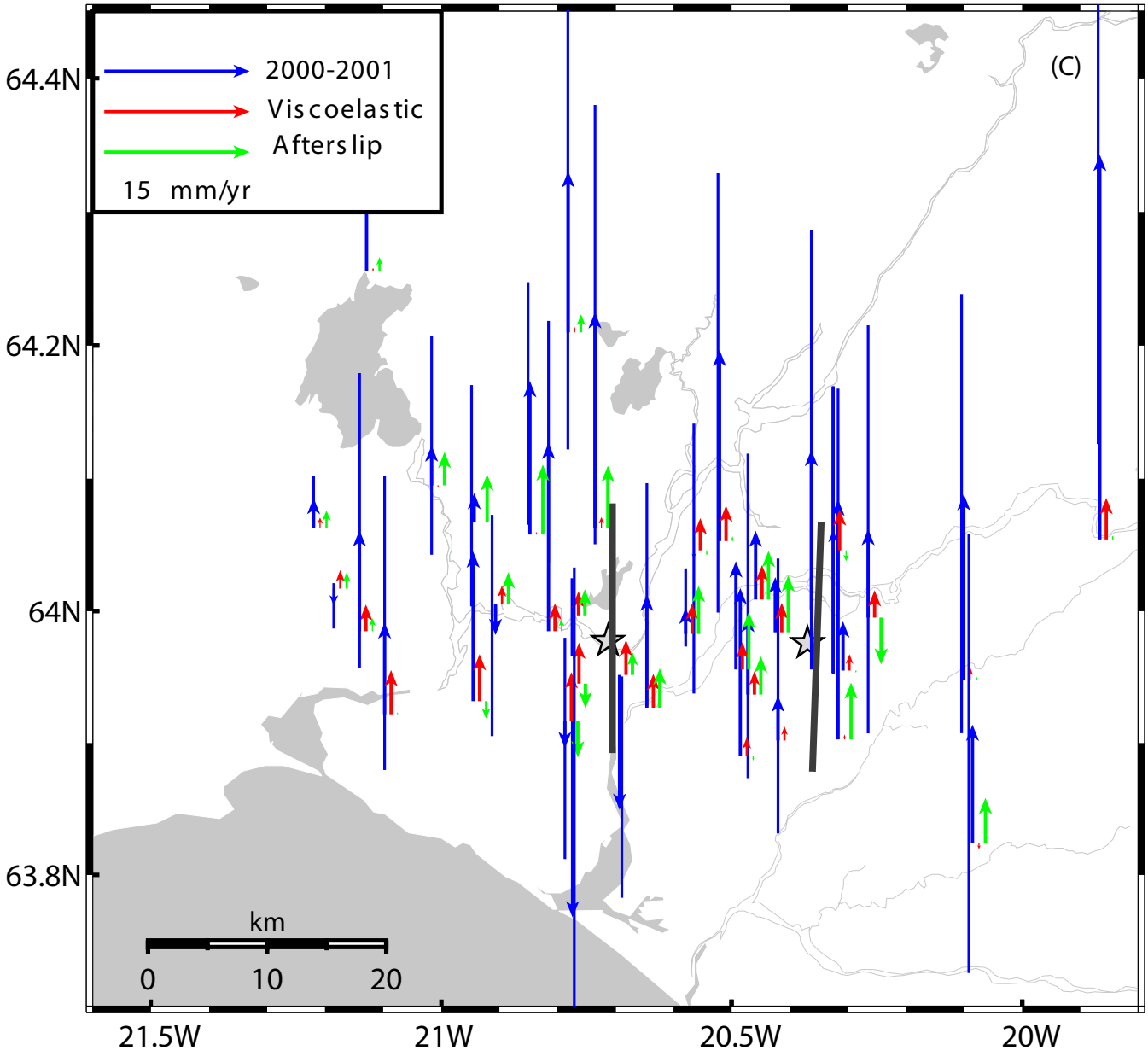

Árnadóttir et al, Figure 9c

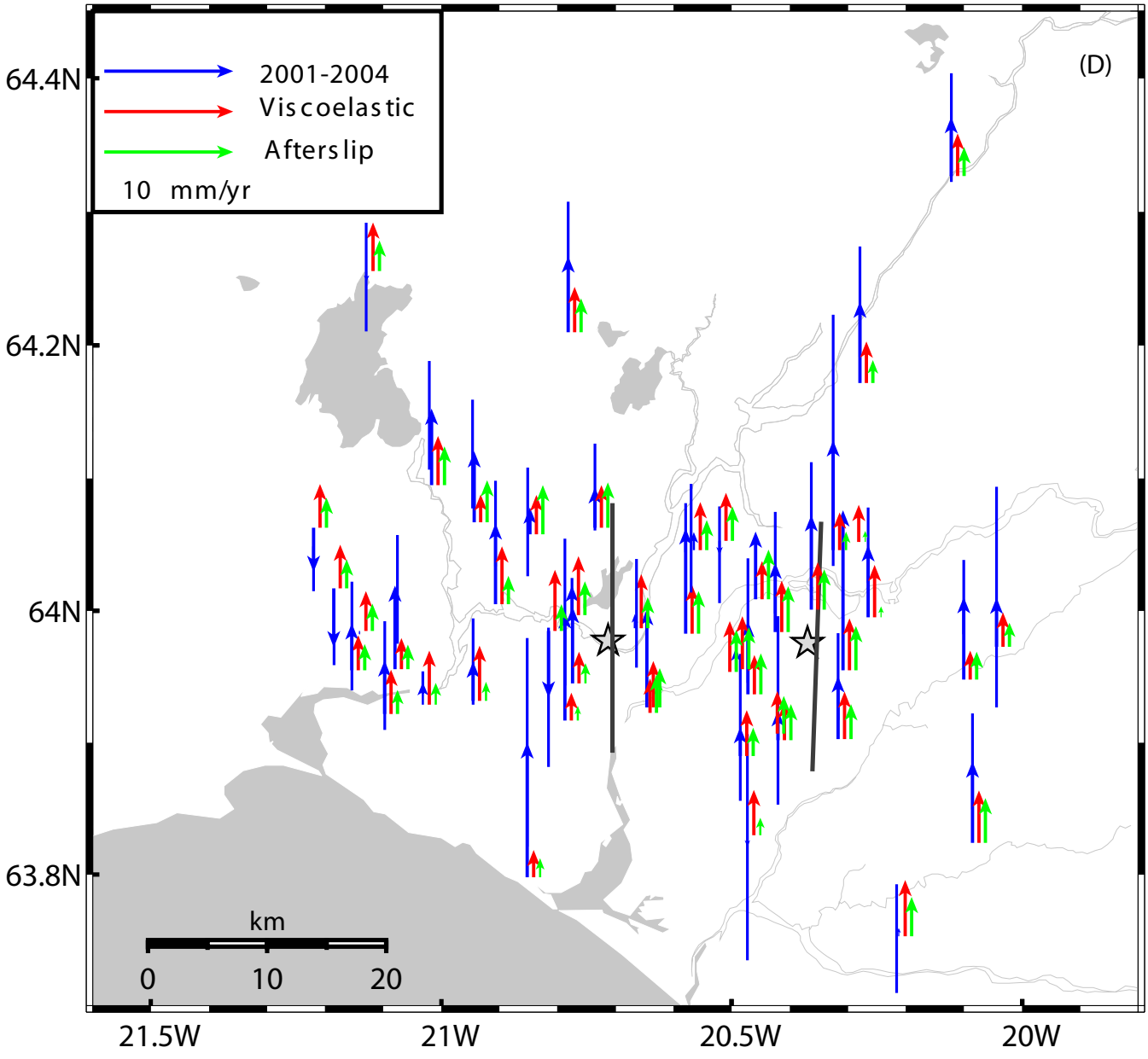

Árnadóttir et al, Figure 9d

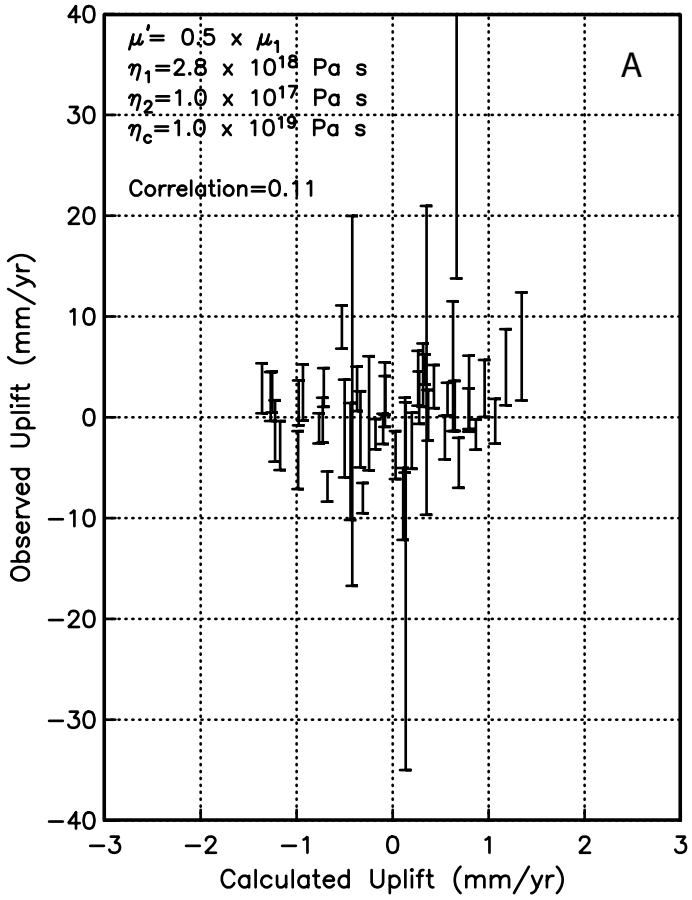

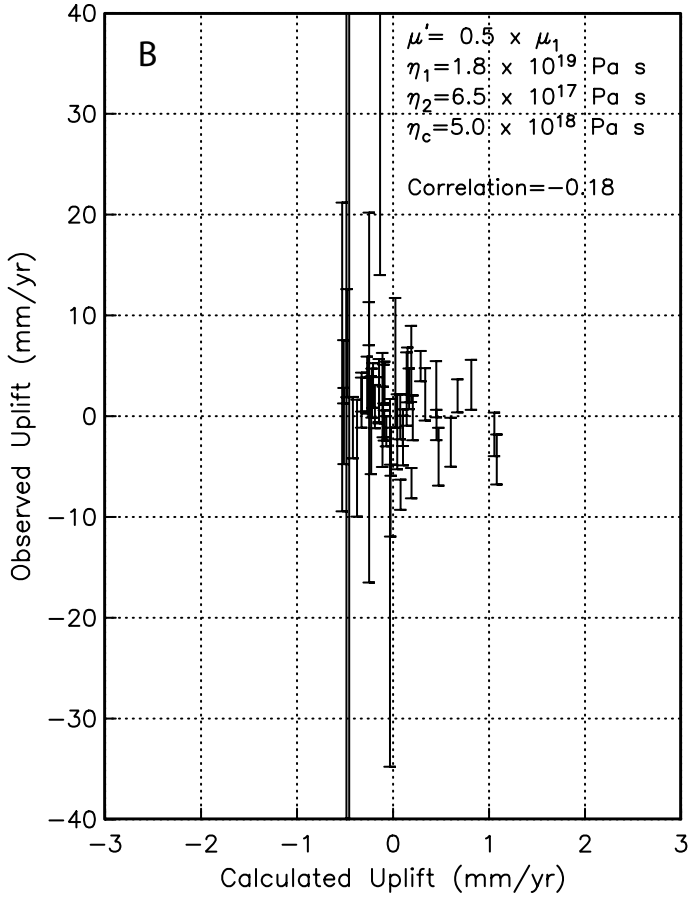

Árnadóttir et al, Figure 10

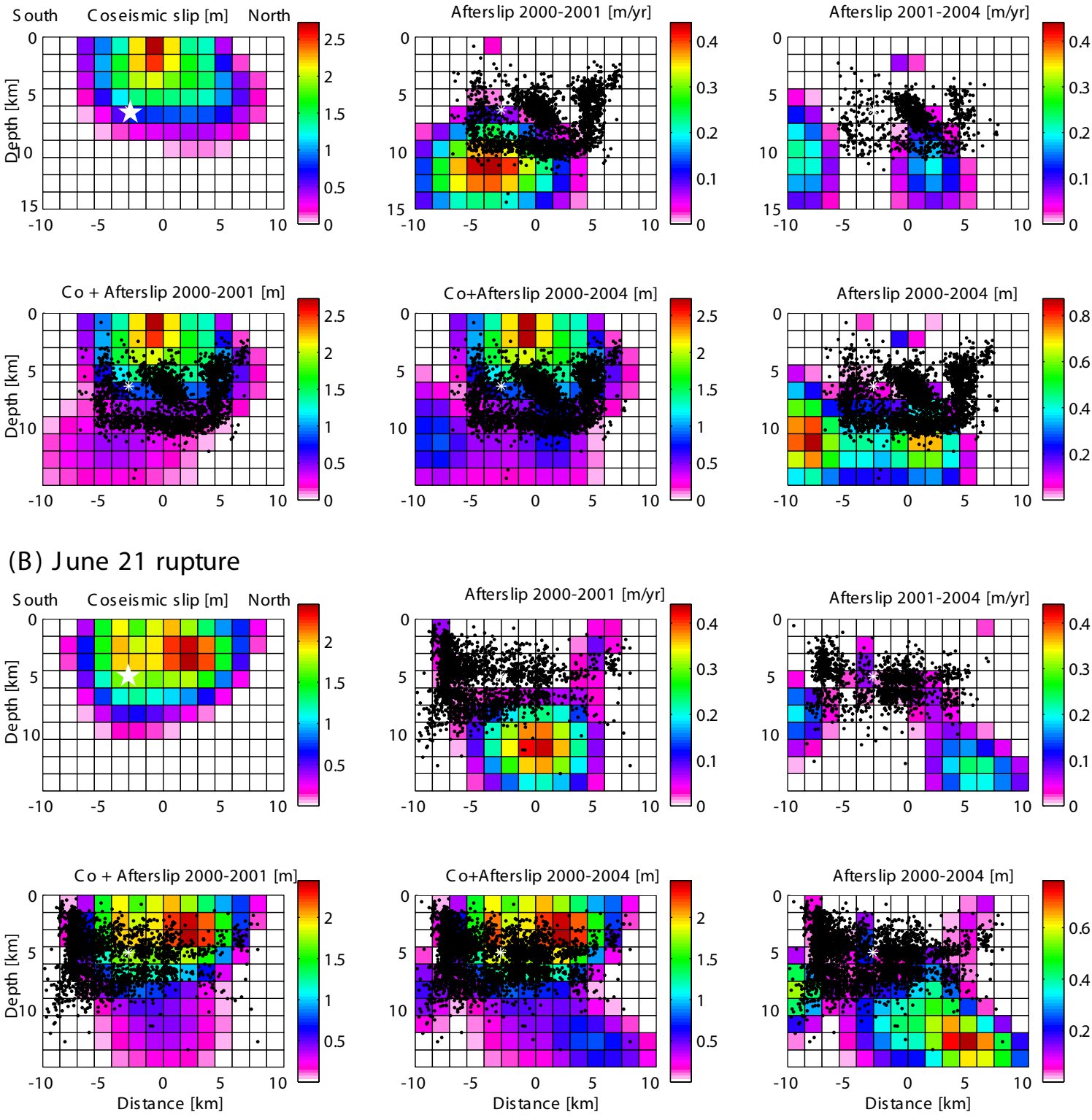

Árnadóttir et al, Figure 11